Feedback loop design and experimental testing for integrated optics with micro-mechanical tuning

by

Laura A. Waller

Submitted to the Department of Electrical Engineering and Computer Science

in Partial Fulfillment of the Requirements for the Degree of

Master of Engineering in Electrical Engineering and Computer Science

at the Massachusetts Institute of Technology

May 19, 2005

Author_____
Departm d Computer Science
May 19, 2005

Certified by_____
stathis
ofessor
rvisor

Accepted by_____
Smith
..., Department Committee on Graduate Theses

Feedback loop design and experimental testing
for integrated optics with micro-mechanical tuning

by

Laura A. Waller

Submitted to the
Department of Electrical Engineering and Computer Science
May 19, 2005

In Partial Fulfillment of the Requirements for the Degree of
Master of Engineering in Electrical Engineering and Computer Science

ABSTRACT

I designed a capacitive sensor with feedback control for precision tuning of a MEMS controlled wavelength-selective switch. The implementation is based upon a customized feedback loop with a PID controller. The positional stability of the bridge can be controlled to within 0.5Å, and the tuner has a time constant of 1μs for the desired 5V actuation voltages. I created a realistic noise model for the capacitive sensor circuit and its controller, and added this to the noise models already developed for the device. Using these models, the parameters of the system can easily be changed to model device performance under varying conditions and device iterations. I also developed an equipment test set-up for accurately measuring the optical properties, both spectral and temporal, of these devices. The apparatus can be modified slightly to be used in testing of other integrated optoelectronic devices. The procedure for aligning lensed fibers to integrated waveguides and optimizing light throughput is described, and some test device values are presented.

Thesis Supervisor: George Barbastathis
Title: Assistant Professor, Massachusetts Institute of Technology, Department of Mechanical Engineering

Acknowledgments

I would like to thank, first and foremost, my thesis advisor, Professor George Barbastathis, for his guidance and teaching. I have learned a lot from my work on this project, and have greatly expanded my research skills. I would like to recognize my colleagues who have worked with me, especially Satoshi Takahashi and Gregory Nielson. Peter Rakich was invaluable in helping me to design and construct the experimental apparatus of Chapter 5, and Professor Mike Perrot lent his knowledge and expertise to the noise analysis developed in Chapter 4.

This research was sponsored by the Defense Advanced Research Projects Agency (DARPA), under the Electronic and Photonic Integrated Circuits (EPIC) project. I am proud to be a part of the project and thank all those involved for their support.

This thesis is dedicated to my mother, who made me who I am, and to my father, who got me started as an electrical engineer. Although my father died while I have been at MIT, the things he taught me have made this thesis possible.

Table of Contents

List of Figures *11*

1. Introduction *13*

1.1. Background 13

1.2. Electronic and Photonic Integrated Circuits (EPIC) Project 14

1.3. Previous work 15

1.4. Motivations and objectives 17

1.5. Tuning 19

1.6. Outline 20

2. Capacitive sensing *21*

2.1. Capacitive sensing 21

2.2. Design of plates 22

2.3. Three-electrode design 24

2.4. Guard and shield electrodes 26

2.5. Sensor Circuit 27

2.6. Limits on performance 30

3. Feedback Control Design *33*

3.1. Feedback loop design 33

3.2. PID controller 34

3.3. Elimination of derivative control 37

3.4. Controller tuning 38

3.5. Circuit Implementation 42

4. Noise analysis *45*

4.1. Noise in integrated circuits 45

4.2. Noise model 47

4.3. Noise in capacitive sensor circuit 49

5. Experimental apparatus for testing integrated optical devices *53*
5.1. Equipment set-up **53**
5.2. Alignment **54**
5.3. Wafer edge facets **57**
5.4. Polarization Dependence **59**
5.5. Ring resonators **60**
5.6. Optical performance tests **60**
5.7. Losses **62**
5.8. MEMS speed tests **64**

6. Conclusions and future work *67*
6.1. Conclusion **67**
6.2. Future work **67**

Appendix A: Control system SIMULINK model *73*
Appendix B: Thermal plant SIMULINK Model *75*
Appendix C: Process flow for diesaw assisted cleaving of wavers *77*

List of Figures

Figure 1: EPIC Phase I ADC schematic 15
Figure 2: MEMs controlled wavelength-selective switch [2] 16
Figure 3: Prototype of device [2] 16
Figure 4: Spectral response when filter on (Nielson 2004) 17
Figure 5: Spectral response when filter off (Nielson 2004) 17
Figure 6: Comparison with currently available RF MEMs switches (Kaertner 2004) 18
Figure 7: Parallel plate capacitance 21
Figure 8: Capacitance of sensor for different electrode sizes 23
Figure 9: Three electrode model [2] 24
Figure 10: Stiffness to area ratio v. maximum control voltage 26
Figure 11: Low impedance two-electrode amplifying circuit 28
Figure 12: Low impedance three-electrode amplifying circuit 28
Figure 13: High impedance amplifier circuit 29
Figure 14: Basic capacitive sensing circuit 30
Figure 15: Model of device control [2] 33
Figure 16: Root locus and Bode plot of device model 35
Figure 17: Bode plot of noiseless PID plus device 36
Figure 18: Step response for PID controller 37
Figure 19: PI controller response to two pulses 38
Figure 20: Root locus of PID controller 40
Figure 21: Closed loop analysis 40
Figure 22: Root locus, step response, and closed-loop bode plot for fast controller 41
Figure 23: PID circuit (SPICE) 43
Figure 24: PID controller circuit 44
Figure 25: RMS noise for varying pull-in voltage 47
Figure 26: Simulink model of device noise 48
Figure 27: Capacitive sensor circuit with noise models 49
Figure 28: Noise in simulated system 51
Figure 29: Test equipment set-up 53
Figure 30: Device alignment equipment 55
Figure 31: Aligned fiber tip and waveguide 56
Figure 32: Cleaved waveguide edges 57
Figure 33: SEM image of one waveguide edge 58
Figure 34: Waveguide polarization sensitivity [12] 59
Figure 35: Ring resonator design 61
Figure 36: Fiber to fiber coupling 62
Figure 37: Waveguide imperfections 64
Figure 38: MEMs switching speed tests 65

1. Introduction

1.1. Background

Optical Integrated Circuits (OICs) research has been ongoing since the 1970s, in an attempt to create smaller, faster, and cheaper optical components for use in communications networks, CMOS chips, and possibly optical computers. OICs contain optical systems, built on a single substrate, with waveguides connecting the components. One advantage of these circuits is that there is no free-space transmission of light, which means more direct interaction, less loss, but new complexities due to polarization dependence and fabrication. Ideally, researchers would like to create a library of modular elements such as lasers, modulators, switches, and detectors, which can all be assembled easily on one single substrate to create an OIC, much the same way electronic circuits are designed today.

OICs have not yet been widely implemented, mostly because their free-space counterparts perform better. For example, in the communications industry, optical to electrical to optical signal processing is fast and cheap enough to meet today's needs. However, as data rates increase and bandwidth broadens, these conversions will become insufficient. Signal processing will need to be done entirely in the optical domain to avoid the bottleneck created by electronic circuit speeds. In addition, optical processing can be used in many other ultra-fast high-tech applications, such as high-speed sampling.

This thesis focuses on a novel integrated optical tunable wavelength-selective filter that is controlled by a micro-electromechanical (MEMS) device. Optical MEMS switches have been previously developed: for example, the Lucent micro-mirror array [1], but most offer only free-space routing of light, which generally means greater insertion loss, larger footprints, and no wavelength selectivity. Our device has the advantage of full integration, fully guided light, and tunable wavelength selectivity.

1.2. Electronic and Photonic Integrated Circuits (EPIC) Project

My thesis work was part of a DARPA-sponsored project on Electronic and Photonic Integrated Circuits (EPIC) to develop Gigahertz High-resolution Optical Sampling Technology (GHOST), namely a high-performance photonic analog-to-digital converter (ADC) that operates at 30GSa/s using 7.5 bits. The ADC will have both optical and electrical components, all monolithically integrated in a CMOS-compatible process.

Use of optics has several advantages in ADC sampling technology:

- Extremely high bandwidths
- Removes timing-jitter bottleneck of current electronic ADCs
- Isolation between the optical and electronic signal
- Sensitive phase/timing measurement

The advantages of the GHOST ADC include reduced size and weight due to CMOS integration, fast optical sampling provided by low timing-jitter mode-locked laser (MLL) pulses, and high dynamic-range quantization beyond 7 ENOB. The product could be used in both radar and communications systems, and will also add to a comprehensive library of highly compact, ultra-fast, modular optoelectronic devices that can be rapidly assembled into custom OICs.

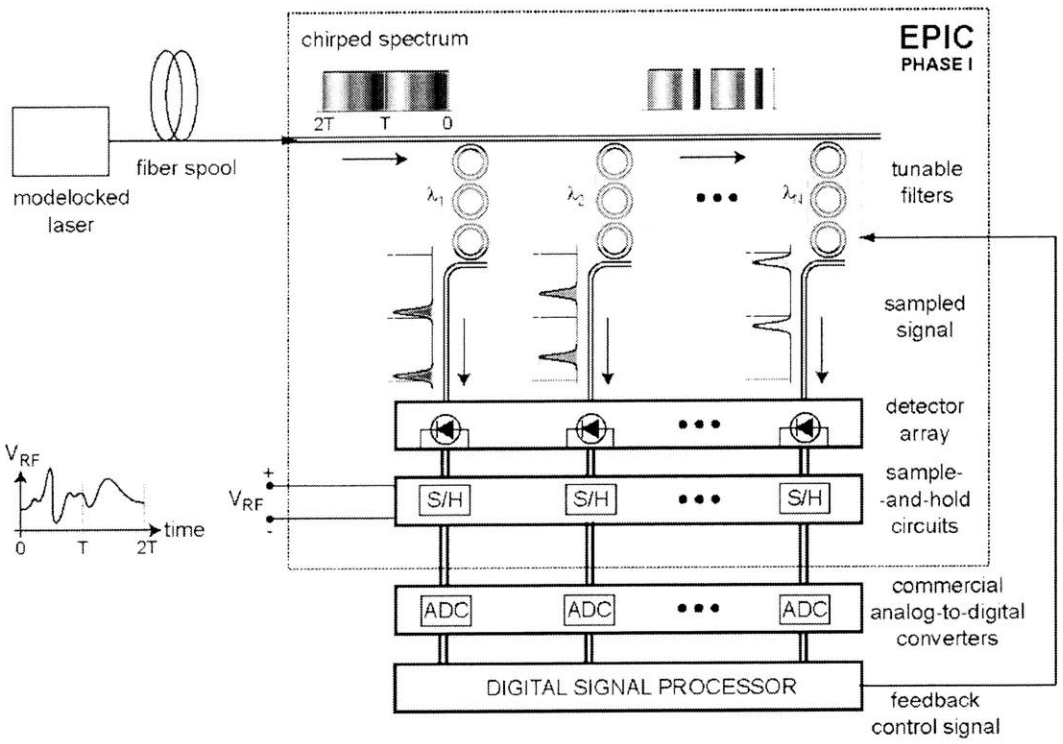

Figure 1: EPIC Phase I ADC schematic

A schematic for the architecture of the ADC is given in Figure 1. Light is introduced to the system via a mode-locked laser, and then dispersed through a long spool of fiber to create a chirped spectrum covering the desired frequencies. M (approximately 20) channels of wavelengths are then picked off simultaneously by third-order tunable filters, and sent to a detector array which converts back to the electrical domain for parallel analog-to-digital conversion of all channels. The total sampling rate is the optical clock rate times the number of Wavelength Division Multiplexed (WDM) channels, M x f_R. This thesis is focused on the wavelength-selective tunable filters of this system.

1.3. Previous work

In his PhD thesis [2], Gregory Nielson designed and fabricated a MEMS-controlled wavelength selective switch, shown in Figure 2. The switch is based on a ring resonator filter. Waveguide 1 carries information on many different wavelengths. The ring resonator then evanescently couples one specific wavelength channel into

Waveguide 2, the drop port. The rest of the wavelengths are passed through on Waveguide 1.

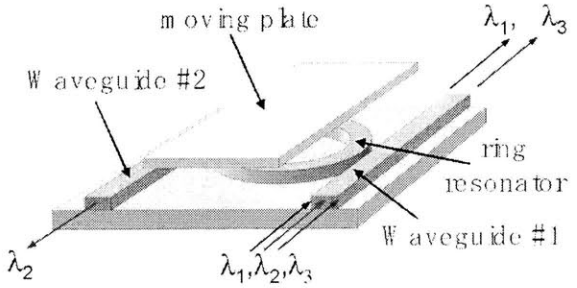

Figure 2: MEMS controlled wavelength-selective switch [2]

An SEM image of a prototype device is shown in Figure 3 below.

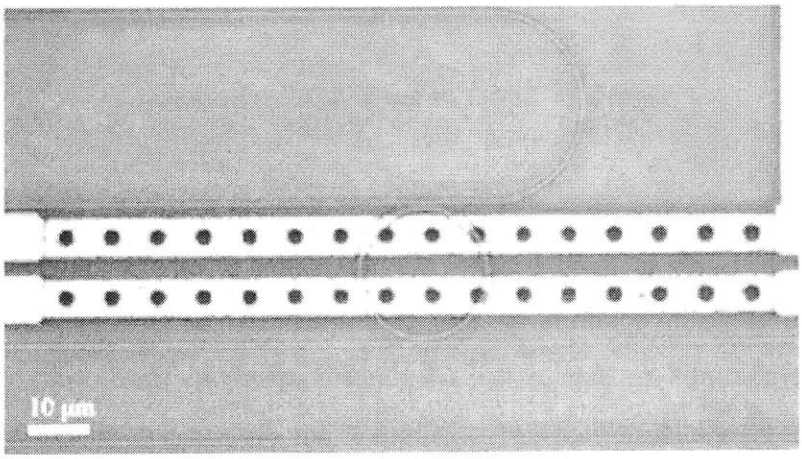

Figure 3: Prototype of device [2]

A parallel-plate MEMS device has been fabricated above the ring resonator, such that it can be suspended above the waveguide device, or can be actuated down close to the ring resonator, within the evanescent field of the filter. Moving the lossy material near the ring resonator introduces damping to the ring resonator. This effectively turns off the dropping function of the device (i.e. all wavelengths are allowed to pass through). Through and drop port spectral characteristics are given in Figure 4 and Figure 5.

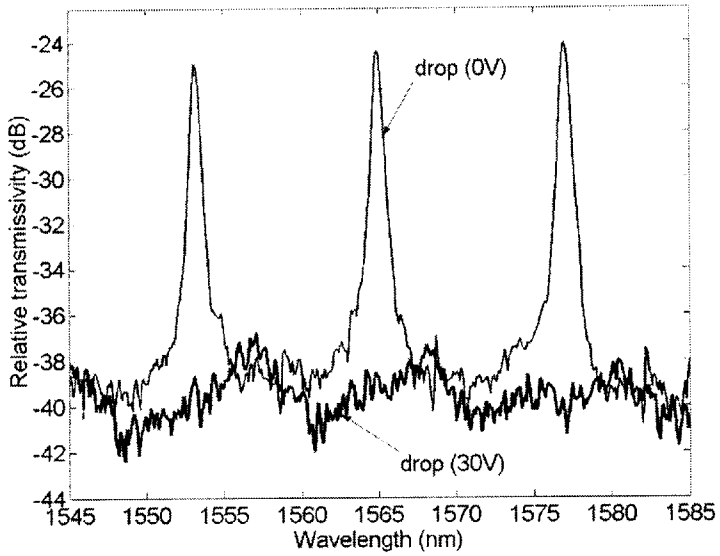

Figure 4: Spectral response when filter on (Nielson 2004)

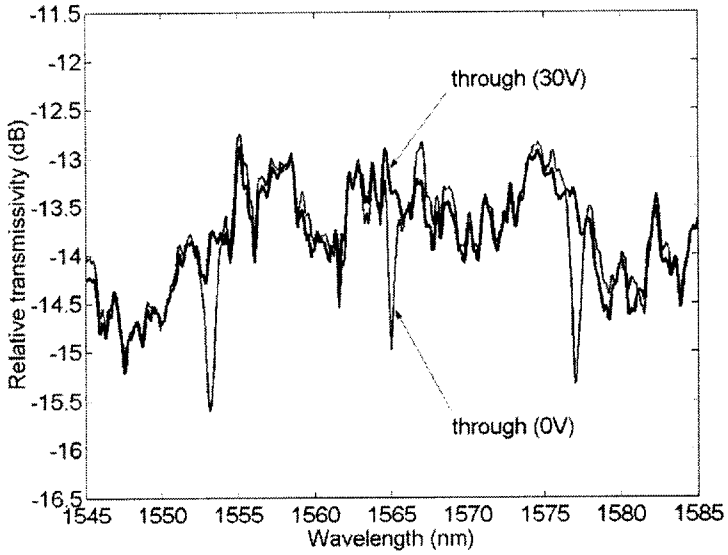

Figure 5: Spectral response when filter off (Nielson 2004)

1.4. Motivations and objectives

These devices not only have application in the GHOST ADC, but also in telecommunications applications, for example, in Reconfigurable Optical Add-Drop Multiplexers (ROADMs). They operate at much higher switching speeds and lower actuation voltages than currently available RF MEMS switches (see Figure 6).

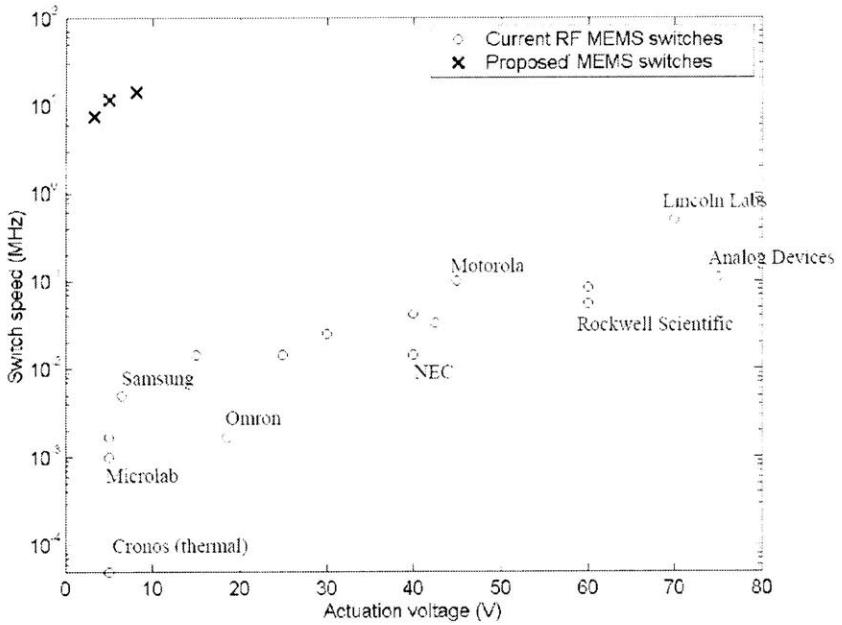

Figure 6: Comparison with currently available RF MEMS switches

The high resolution required of passive WDM filters for ultra-fast sampling imposes very strict constraints on the mean frequencies of the interleaved channels, the converter gains, and the sample memory effects. Precise timing of the clock signals requires frequency stability, which can be readily adjusted with integrated feedback control of the filter resonance wavelength. The main goal of this thesis is to modify the design of Neilson's device to make it wavelength tunable. The desired specifications for the tunable device are given below in Table 1.

Table 1: Device parameter goals

Parameter	Specification
Actuation voltage	5V
Wavelength tuning range	30nm 100GHz
Displacement Stability	+/- 0.07nm
Tuner response time	<1ms

1.5. Tuning

In the GHOST project, fast feedback control of the filter wavelength reduces timing jitter and therefore enables high resolution sampling. A wide tuning range allows dynamic redistribution of the filter wavelengths between the dropped channels.

There are several possible methods of wavelength tuning. The basic goal is to change the optical path length of the light in the ring resonator. Changing the physical dimensions of the ring dynamically is one option pursued by Wong of MIT [3]. The best way to achieve tuning is by changing the effective refractive index of the ring. This can be done several ways:

- carrier injection – The system losses for carrier injection are high and only a limited tuning range is achievable (~5nm).
- thermo-optic tuning – Thermo-optic tuning is not energy-efficient, is usually very slow, and requires large circuits to control it.
- MEMS tuning – Using MEMS for tuning is fast, offers a large tuning range (~100nm), and is easy to implement.

This thesis will investigate the MEMS implementation. If the MEMS bridge of the previously discussed switch is fabricated with a suitable dielectric material, its presence near the ring resonator device will alter the optical path traversed by light in one round-trip.

Thus, the wavelength selection is determined by d, the distance of the MEMS bridge from the control electrode. In order to tune the device over the full free spectral range (FSR), approximately 30nm, we must be able to accurately control the bridge within the range of 50-500nm above the ring resonator filter. The wavelength resolution required grows exponentially with increasing distance between the filter and the bridge. At 50nm, the bridge must be positioned within 0.7Å of stability. Neilson (Nielson 2004) showed that this is impossible to do with open loop control, due to Brownian noise and

stray capacitances and suggested the use of feedback. The required feedback system is the core of this thesis.

1.6. Outline

Chapter 2 starts with a brief study of capacitive sensors and their advantages in our device. The design of an integrated capacitive sensor to be used for the tuning of the wavelength selection in the device is also shown. Chapter 3 presents the design of a feedback controller to reduce error and improve speed of the system. In Chapter 4, improved and expanded noise models and simulations for the system are shown. A test setup for measuring optical temporal and spectral characteristics of integrated optics devices was developed as part of this thesis work. The apparatus and preliminary results are shown in Chapter 5. Conclusions and suggestions for future work are given in Chapter 6.

2. Capacitive sensing

2.1. Capacitive sensing

Capacitive sensing is widely used in industry in flow meters, pressure sensors, liquid level sensors, and spacing and thickness measurement. The basic idea of capacitive sensing is to use the measure of change of capacitance between two or more electrodes to determine characteristics of the material or spacing between them.

Two parallel plate electrodes will have a capacitance between them that is directly proportional to the distance between them, d. A schematic of a basic capacitive sensing circuit is shown in Figure 7. It is assumed that the plates will be relatively close together, such that the distance between them is smaller than their dimensions and fringing is negligible.

$$C = \frac{\varepsilon_0 \varepsilon_r A}{d}$$

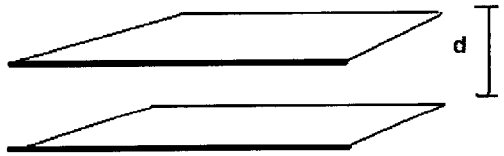

Figure 7: Parallel plate capacitance

ε_0=8.854 x 10^{-12}, and ε_r=1.006 in air, and 1 in a vacuum.

Capacitive sensing has been shown to be excellent for highly accurate positional control in micro devices. Motion detectors can detect displacements as small as 10^{-14}m with good stability, high speed, and good tolerance to wide variations of environmental

factors [4]. Capacitive sensing has been proven to be a low-cost, very stable, and simple implementation.

Capacitive sensing is particularly convenient for our device, as the MEMS bridge itself can act as one electrode, whereas a second electrode can be built on the substrate. Measurement of the capacitance between these electrodes will allow accurate measurement and control of the bridge position with little susceptibility to environmental changes, excluding humidity.

Design of the capacitive sensor for this device was done in five steps. First, the plates were designed around the device to achieve maximum capacitance with minimal complexity, and then the guard/shield electrodes were designed to handle stray capacitance and crosstalk. Next, the sensor capacitances, stray capacitances, and output signal swing were calculated to ensure they met specifications. The transfer function of the sensor was then found, and the excitation frequency was chosen accordingly to be high enough to minimize noise effects on the measurement.

2.2. Design of plates

The graph in Figure 8 shows the capacitance at the sensor for a circular sensor at the ring, and a smaller and larger rectangular sensor. It is desirable to place the sensor electrodes as close to the center of the device as possible, without interfering with device operation. The 25x40 μm^2 sensor will give the best performance and can be placed at the edges of the ring resonator for best performance.

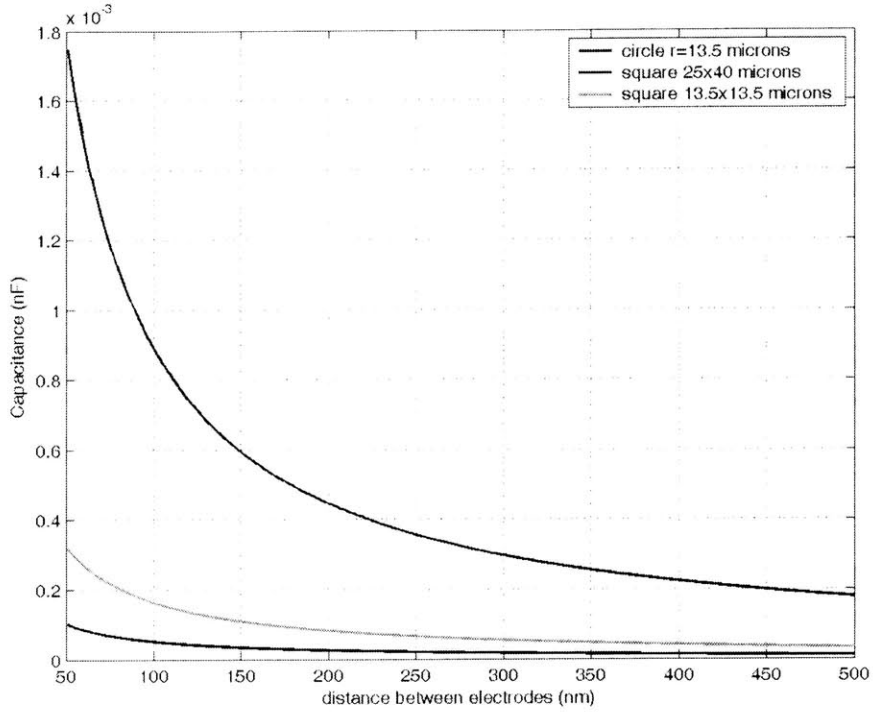

Figure 8: Capacitance of sensor for different electrode sizes

As can be seen in Figure 8, the capacitance is largest at the smallest spacing between the electrodes, and varies exponentially with distance. To eliminate this non-linearity, we can measure the capacitance impedance instead, since this dependence on electrode spacing is linear. The capacitive impedance Z is:

$$Z = \frac{1}{2\pi fC}$$

Parallel plate sensors have unwanted sensitivity to transverse displacement, coupling from the back of the plate, and tilt. To improve performance due to transverse displacement, many sensors could be built next to each other to measure capacitance in parallel. The rationale for this design is that random, uncorrelated transverse displacements in adjacent electrodes should cancel each other out after a sufficiently long integration time. However, in our device, transverse displacement should not occur, whereas, increasing the complexity of the sensor circuit would reduce the fabrication

yield and create extra noise in the feedback loop. Thus, it was decided that a single sensor is sufficient.

2.3. Three-electrode design

Neilson [2] proposed the three-electrode actuator design shown in Figure 9. The benefit, in addition to the actuation advantages mentioned earlier, is that adding electrodes increases the capacitance of the sensor, and thus the sensitivity. The device can measure 0.0018nF of capacitance with a single parallel-plate sensor. We would like to increase the capacitance of the sensor without unduly complicating the fabrication process. The three-electrode model doubles the sensor capacitance, first-order compensates for tilt, reduces errors due to circuit drift, and makes shielding easier. More accurate positional control can be achieved using lower actuation voltages.

The detecting circuit will measure the ratio of the bridge capacitance to the top and the bottom electrode. No absolute capacitance reference is needed, and the motion and capacitance relationship will be parabolic.

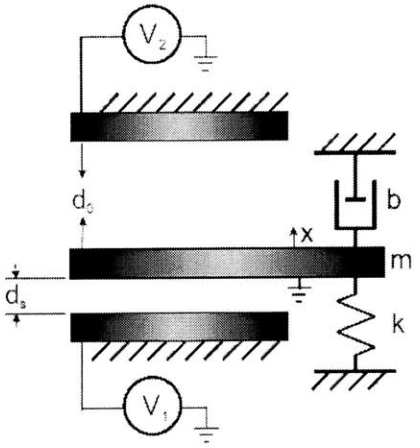

Figure 9: Three electrode model [2]

An ideal design places the unactuated bridge 50nm above the ring resonator, and the third fixed electrode at 500nm above the ring resonator. These unequal distances

exploit the nonlinearities in the wavelength resolution required at different distances from the filter; the finest control is needed near the initial position. Since the sensing electrode has the highest sensitivity when plates are in close proximity, it is most efficient to use the bottom electrode as the sensing electrode.

A sinusoidal sensing signal of much lower frequency than the natural frequency of the system is applied to the bottom/sensing electrode, effectively applying a DC voltage of

$$V_s = V_{s0}\sin(\omega_s t)$$

A control voltage, the bias voltage plus the reference voltage, is applied to the top/control electrode

$$V_c = \sqrt{\frac{2kx(d_0 - x)^2}{\varepsilon_0 A} + \frac{{V_{s0}}^2 (d_0 - x)^2}{2(d_s + x)^2}}$$

The equation for motion of this model is

$$m\ddot{x} + b\dot{x} + kx = \frac{\varepsilon_0 A {V_c}^2}{2(d_0 - x)^2} - \frac{\varepsilon_0 A {V_s}^2}{2(d_s + x)^2}$$

The control voltage is chosen to be at V_2, and the sensing voltage at V_1. d_0 denotes the initial gap between the top two electrodes, and A is the area of overlap.

The pull-in voltage is set to the maximum actuation voltage, 5V in our ideal design. The pull-in voltage determines the stiffness to area ratio, the maximum control voltage, and the sensing voltage.

By increasing the pull-in voltage, we can exponentially increase the stiffness to area ratio, k/A, exponentially (see Figure 10). This allows the use of a higher stiffness material and/or a lower area of overlap. We always want to maximize the area of overlap for the device.

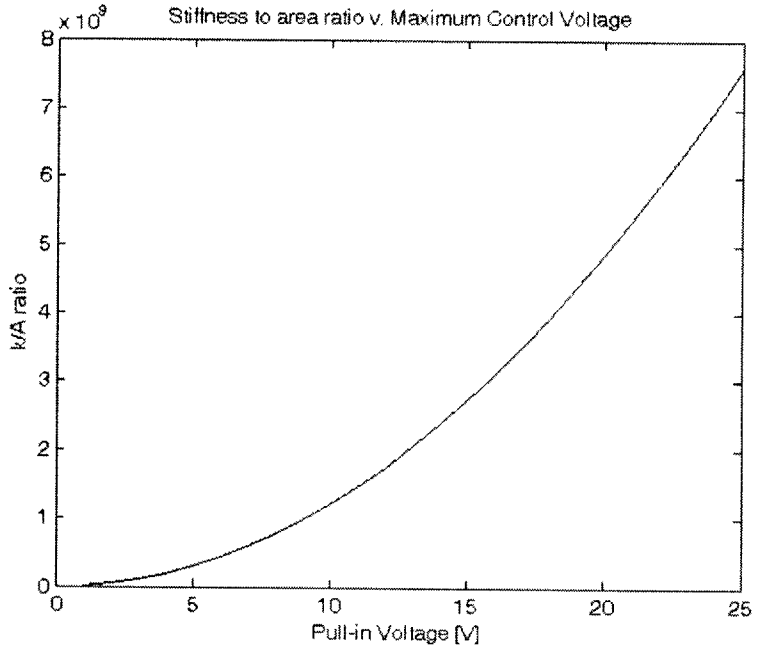

Figure 10: Stiffness to area ratio v. maximum control voltage

2.4. Guard and shield electrodes

The goal of shielding is to build a conductor that surrounds the sensor, in order to shunt the capacitive current to ground without affecting the sensor. When working with sensors with capacitance in the pF range, as we are, shielding becomes essential to avoid out-of-band signals saturating the input amplifier. A shield will attenuate magnetic and electric fields, and its effectiveness is determined by the sum of its absorption and reflection according to

$$S = 8.69\left(\frac{d}{\delta}\right) + 322 - 10\log\left[f^3 r^2 \frac{\mu_r}{\sigma_r}\right] \quad [\text{dB}]$$

d = thickness

δ = skin depth

f = frequency

r = distance between shield and source

$\frac{\mu_r}{\sigma_r}$ = ratio of permeability of shield to conductivity of shield [5]

For a copper shield of 0.420mm thickness (one skin depth) close to the source, all practical external fields will be effectively attenuated within a reasonable frequency band.

A guard is a shield that is connected to the common-mode potential of the signal being processed . By using a combination of guards and shields, stray capacitance and external noise can be all but eliminated.

I propose here to use a copper guard ring to reduce surface currents. A guard ring is a conductor placed around the perimeter of each sense electrode to shield the sensor from external currents. The thickness will be determined by the measured external field noise in the actual device.

2.5. Sensor Circuit

The sensor circuit converts the sensor capacitance into a voltage or current. It is desired to have good linearity, robustness against stray capacitances, low noise, and a reasonably large signal bandwidth.

The simplest two-electrode model low impedance circuit is given below in Figure 11.

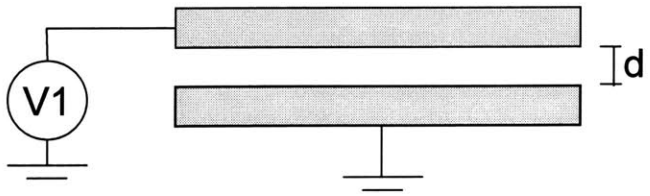

Figure 11: Low impedance two-electrode amplifying circuit

Where

$$I_{out} = \frac{V_I}{Xc} = V_I \omega (8.854 \times 10^{-12})$$

With the third electrode, the circuit becomes that shown below in Figure 12, with

$$I_{out} = V_I \omega (8.854 \times 10^{-12}) \frac{2x}{d_0^{\,2}}$$

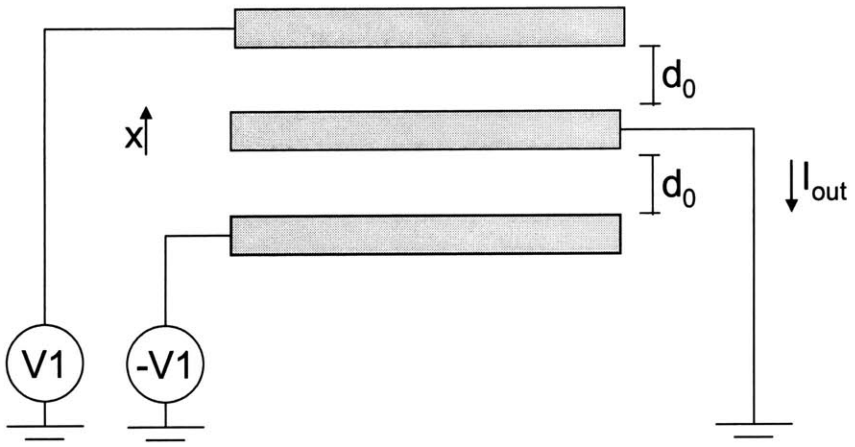

Figure 12: Low impedance three-electrode amplifying circuit

A high impedance amplifying circuit could also be used (Figure 13). The voltage output it gives will no longer be nonlinear, the electrostatic force will be zero, and the circuit has a dependence on the dielectric constant.

$$V_{out} = 2V\left(\frac{X_{C2}}{X_{C1}+X_{C2}}\right) - V_1 = \frac{V_1}{d_0}$$

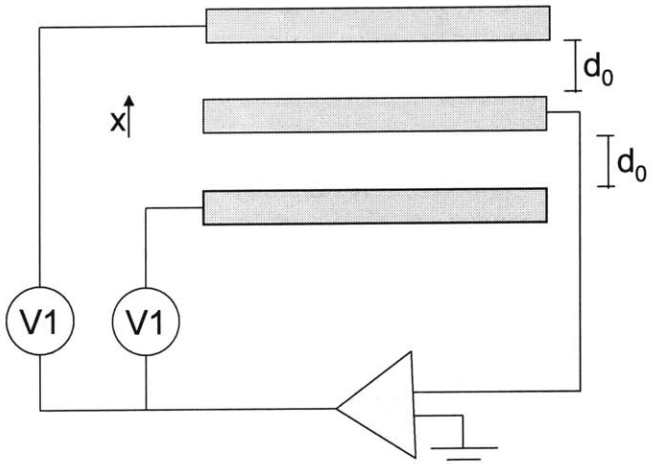

Figure 13: High impedance amplifier circuit

We use a high excitation frequency to get low electrode impedance (1-100mΩ). The excitation waveform can be square or sinusoidal, depending on which is easier to implement. One thing to note, however, is that a square excitation will produce an output bandwidth much higher than the excitation frequency (~10x), rather than the 2x or 3x with sinusoidal excitation. Sensors with a continuous waveshape usually use synchronous demodulators, which have high precision and good rejection of out-of-band interference. The amplifier circuit can be designed to measure C1-C2, C1/C2, or (C1-C2)/(C1+C2).

The basic capacitive sensor circuit is given below in Figure 14. This circuit uses a Schmitt inverter as an RC oscillator, and the output can be either capacitance-linear, or 1/capacitance-liner, depending on where the sensor is placed. Small sensor plates such as ours will have very high impedance circuitry, so the op-amp input impedance will need to be many hundreds of megaohms.

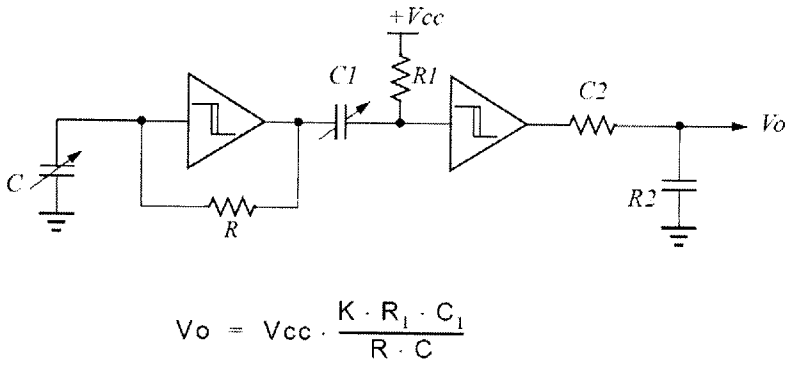

Figure 14: Basic capacitive sensing circuit [4]

2.6. Limits on performance

Capacitive sensors are generally very stable with environment. The effects of temperature and humidity are minute. Edge effects (fringing) will cause less than 3% error for the dimensions given and can be reduced by shields. The main challenge with capacitive sensing is stray capacitance. This can be greatly reduced if the control circuitry is integrated onto the same chip as the MEMS device. In fact, in order to meet the speed and accuracy requirements proposed, the control circuitry *must* be monolithically integrated. This makes fabrication more difficult, but allows desired performance for CMOS actuation voltages of < 5V.

The precision of a capacitive sensor could potentially be limited by the quantization of the electron charges. For the smallest sensor considered and a test voltage of 1V, the number of electrons on the plate will be given by:

$$q = CV = (0.1 \times 10^{-12} F)(1V) \times 6.242 \times 10^{18} electrons / C = 6.242 \times 10^{5} electrons$$

This should be sufficient to limit quantization noise.

The input current noise is another parameter that limits precision of the sensor. Since the capacitive sensor has high impedance (~1.8MΩ at 50kHz), the current noise

factors more than the voltage noise. With ultra-low noise op-amps in the circuit (~0.8 $pA/\sqrt{Hz}$), as discussed in Chapter 4, the signal to noise ratio can be improved by as much as six orders of magnitude.

In real systems, however, circuit noise and thermal noise usually make up most of the system noise. Further noise analysis of the sensor is given in Chapter 4. Despite noise constraints, current sensors have been reported with noise as low as a few thousand noise electrons per second, and with sensitivity as good as $0.01 \times 10^{-19} F$ [8] .

3. Feedback Control Design

3.1. Feedback loop design

The system is nonlinear, but can be linearized about a certain operating point for initial feedback control, then later expanded to nonlinear control as needed. Feedback will eliminate negative effects of some fabrication and temperature/time variations.

A basic layout of the feedback system is given in Figure 15.

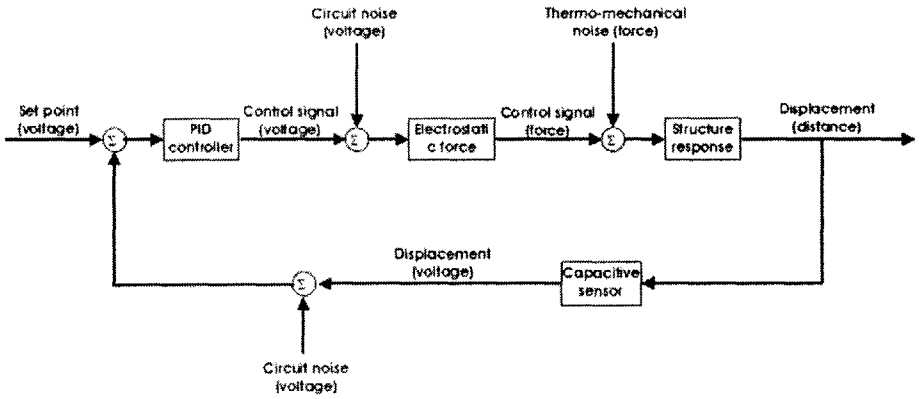

Figure 15: Model of device control [2]

The feedback circuit will require robustness, calibration, and possibly further analysis of system characteristics. As always, fabrication and noise will benefit from greater simplicity in the feedback loop. Noise sources include mechanical vibrations, thermal mechanical noise, Brownian noise, electronic signal noise, and stray capacitances and will be discussed in the next chapter.

The control system was designed around one particular operating point. In order to make it more robust and effective, there are several possible methods of nonlinear control. Several controllers can be designed around varying operating points, and switching between these would allow piecewise linear control. Alternatively, we could

use the controller to compensate for the nonlinearity. By taking the input as voltage squared, we can cancel out the square nonlinearity in the system.

3.2. PID controller

PID (proportional plus integral plus derivative) control is the standard form of dynamic compensation for a feedback circuit. They can be bought off the shelf to meet specifications, but we will build the simple circuitry externally as a prior to the integrated controller which will be included in the final device. Since the device will be integrated, reducing complexity is a priority, as is controller speed, and keeping the gain parameters as low as possible.

The transfer function for a PID controller is given below. K_p is the proportional gain, K_i the integral gain, and K_d is the derivative gain.

$$G(s) = K_p + \frac{K_i}{s} + K_d s$$

The Bode plot and root locus of the device without any controller is given in Figure 16. It is a second order system with a characteristic resonant peak. The bandwidth of the system is 2.91 x 10^5 rad/s at the -3dB point [11], and we want to design a controller with good performance over this range.

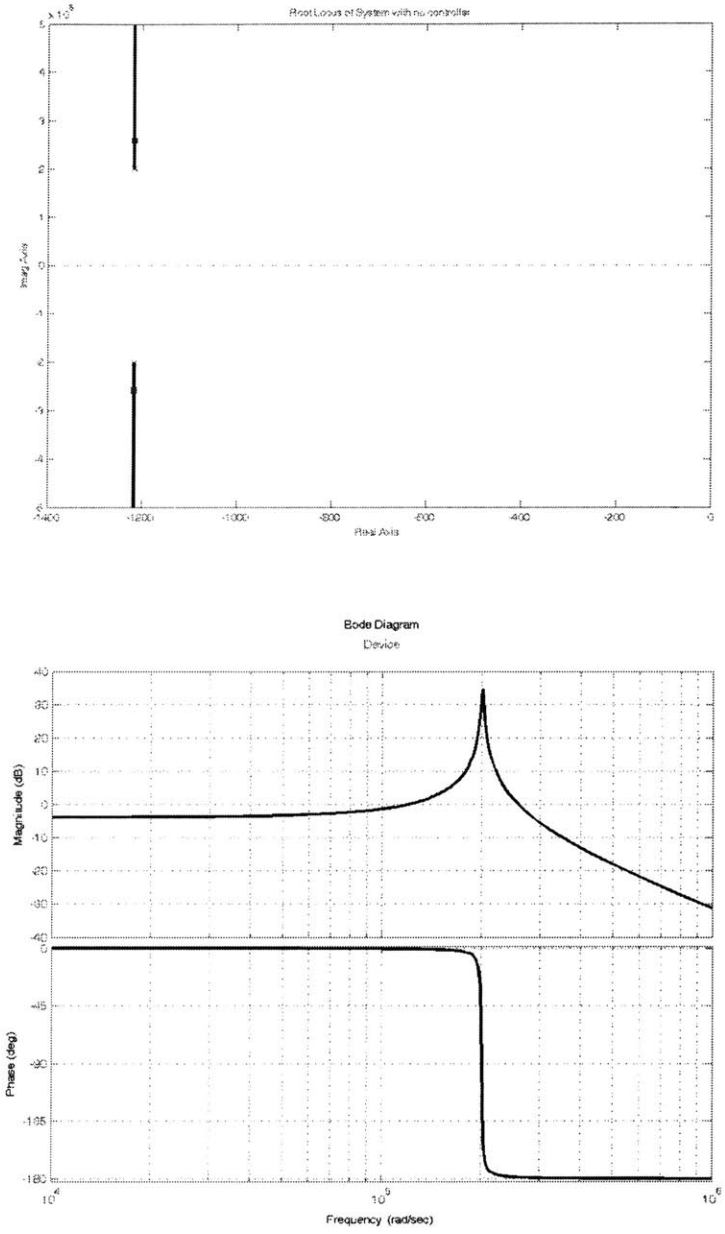

Figure 16: Root locus and Bode plot of device model

The device has the following parameters:

Eigenvalue	Damping	Freq. (rad/s)
-1.22e+003 + 2.01e+005i	6.05e-003	2.01e+005
-1.22e+003 - 2.01e+005i	6.05e-003	2.01e+005

The damping is small, and hence the system will naturally oscillate before coming to a steady state value. Since the plant is of type 0, the steady-state error due to a step input will be nonzero.

We aim to build a compensator with integrator to eliminate steady state error. To do so, we start by placing the zero at the origin, and a pole in the left half plane. The Bode plot of the plant plus a PID controller with no noise is shown in Figure 17 below. It will need to be optimized for speed, oscillations, bandwidth, and gain parameters.

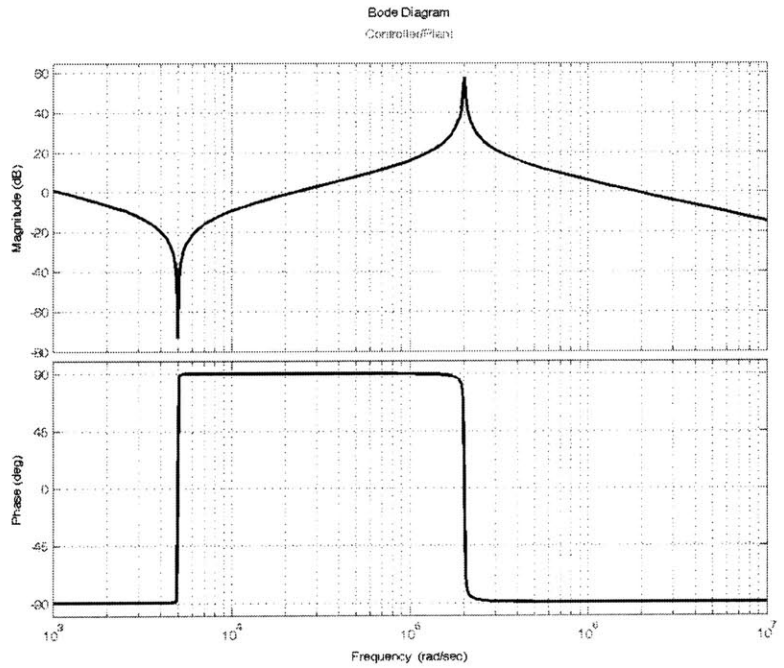

Figure 17: Bode plot of noiseless PID plus device

The transfer function of the device will give us insight to the controller design:

$$\frac{1}{3.84\text{e-}11\ s^2 + 9.35\text{e-}08\ s + 1.555}$$

We can see that there is a range of 11 orders of magnitude in the transfer function. The controller design will be an ill-posed problem. The controller poles will be very far from the device poles on the s-plane, and the controller will require very high gains and/or may suffer from unwanted oscillations.

3.3. Elimination of derivative control

Derivative control reduces the time that it takes for the output to converge to its set-point value, and is only useful, let alone necessary, in somewhat unstable systems where the system oscillates undesirably about its set value.

Figure 18 shows the system with PID controller response to a step function input. The large spike is due to an underdamped response with a very fast time constant, introduced by the controller at moderately high gains. At even higher gains the response becomes overdamped, but unfortunately these required gains are too high to realize.

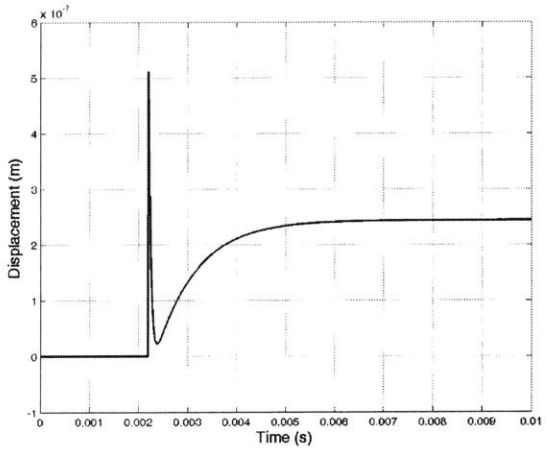

Figure 18: Step response for PID controller

A much more ideal response is obtained for a PI controller (Figure 19), for the same proportional and integral gain values. This is because a PI controller has no imaginary poles or zeros, so there are no oscillations.

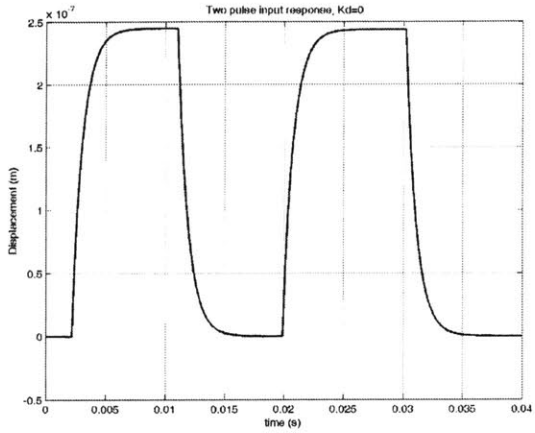

Figure 19: PI controller response to two pulses

Eliminating derivative control will reduce the complexity of the circuit implementation for the controller, which has several advantages. Fabrication becomes easier, the footprint of the device becomes smaller, and the circuit noise from the control circuit will be reduced. The tradeoff is in the speed of the controller. Without derivative control, the system has a 10-90% rise time of 0.002s. With derivative control, the rise time is 0.005s.

It is possible to avoid the spike with derivative control included by carefully placing the controller poles. I will design the system for PID control because we want maximum switching speed in the device; however, it is possible to tradeoff some speed for lower complexity by using PI control only.

3.4. Controller tuning

There are several methods for choosing the gain parameters of a PID controller. One Zeiger-Nichols method is based upon a 25% overshoot in the step response . The integral and derivative gains are set to zero, and the proportional gain is increased until its critical gain, K', where the output shows sustained oscillations of period T' [7]. Then the gains are set to be:

Kp=0.6K',

Ki=1.2K'/T'

Kd=4.8K'/T'

Another approach is to look-up values in a standard table which allows rise time speed to be traded off with delay . I saw better performance by studying the root locus plot and adjusting the poles manually.

It is desirable to place the controller poles close to the real axis to avoid oscillations and far from the imaginary axis for a fast settling time. Of course, we want to do this with minimal gain to save system power.

I wanted to obtain the best performance in four categories: closed-loop bode plot, compensator bode plot, step input response, and step error rejection . In this case, the step response is the most important plot, as that will determine the upper limit on switching speed for the MEMS bridge. For my three-electrode design, I was able to obtain good results with no unwanted oscillations and a step response 10-90% rise time of 0.006s. The root locus for the system and parameters of closed-loop feedback analysis are shown in Figure 20 and Figure 21. The controller in this system has:

$$C(s) = \frac{177(1 + 2\times10^{-7}s + (0.00014s)^2}{s}$$

Which corresponds to Kp = 0.0000354, Ki = 177, and Kd = 0.0000034692. Such small gains may be difficult to obtain in an op-amp circuit with noise.

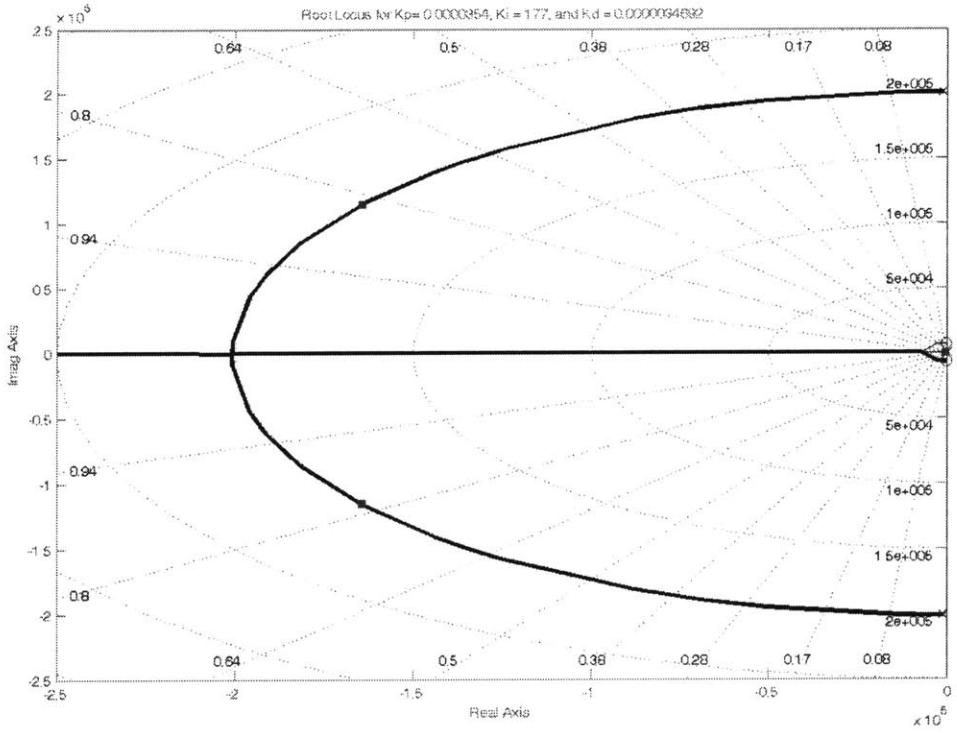

Figure 20: Root locus of PID controller

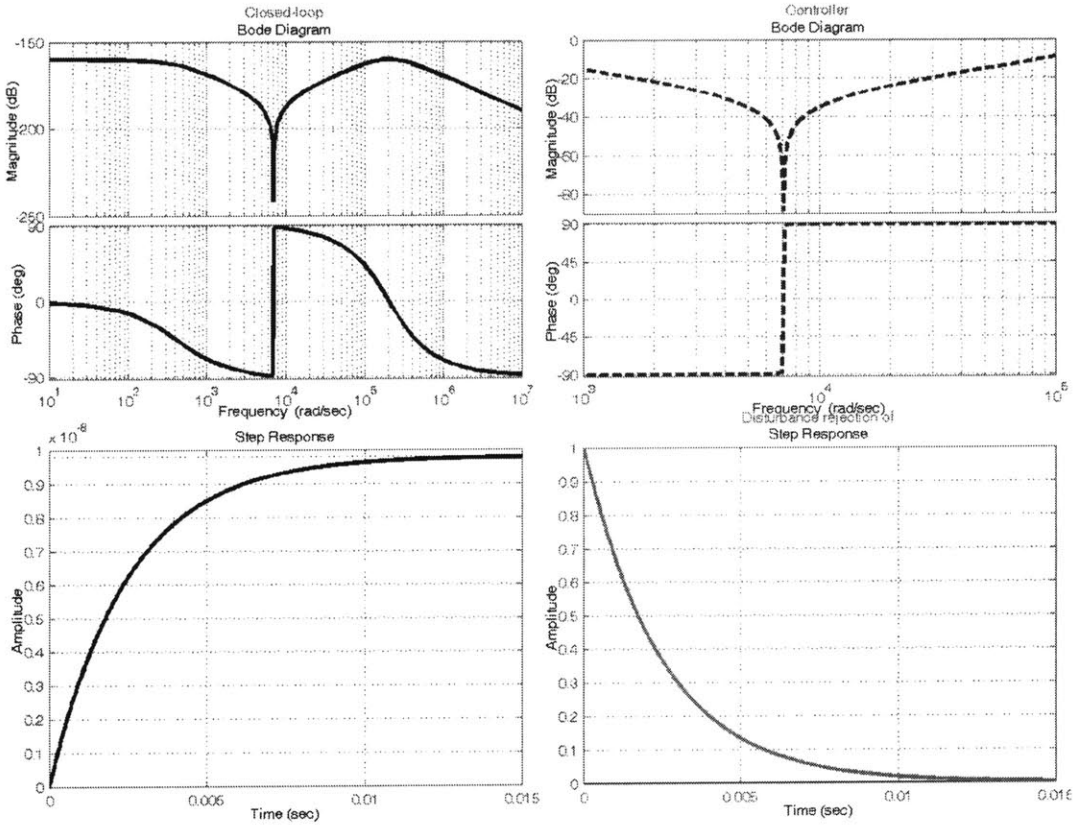

Figure 21: Closed loop analysis

If smooth oscillations and higher gains can be permitted, then the system can be made to have a very fast step response, with a 10-90% rise time of 0.00003s and a larger bandwidth (see Figure 22).

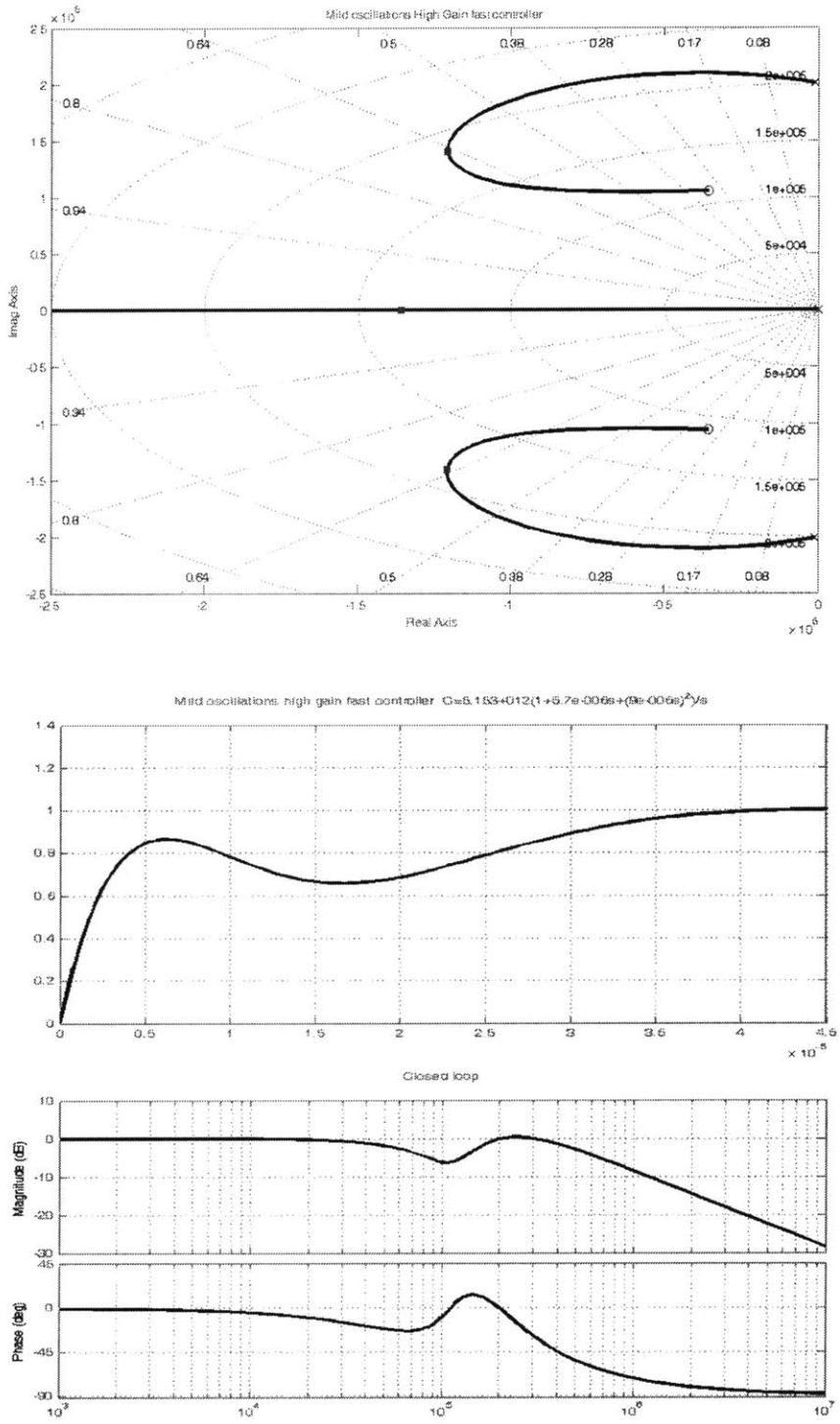

Figure 22: Root locus, step response, and closed-loop Bode plot for fast controller

The controller transfer function of this fast system is:

$$C(s) = \frac{5.153 \times 10^{12}(1 + 5.7 \times 10^{-6} s + (9 \times 10^{-6} s)^2}{s},$$

and the gains are Kp = 29366400, Ki = 5.153×10^{12}, and Kd = 417.393. The integral gain on this system is huge, and will be impractical, unless many stages of amplification are available. A typical op-amp has a gain/bandwidth product of 1000000000.

The final design parameters for the two systems with different characteristics are given in Table 2 below.

Parameter	**No oscillations** (Figure 21)	**Fast system** (Figure 22)
Kp	0.0000354	29366400
Ki	177	5.153×10^{12}
Kd	0.0000034692	417.393
10-90% rise time [s]	0.006	0.00003

Table 2: PID parameter effects

3.5. Circuit Implementation

A SPICE circuit implementation for a PID controller is given in Figure 23.

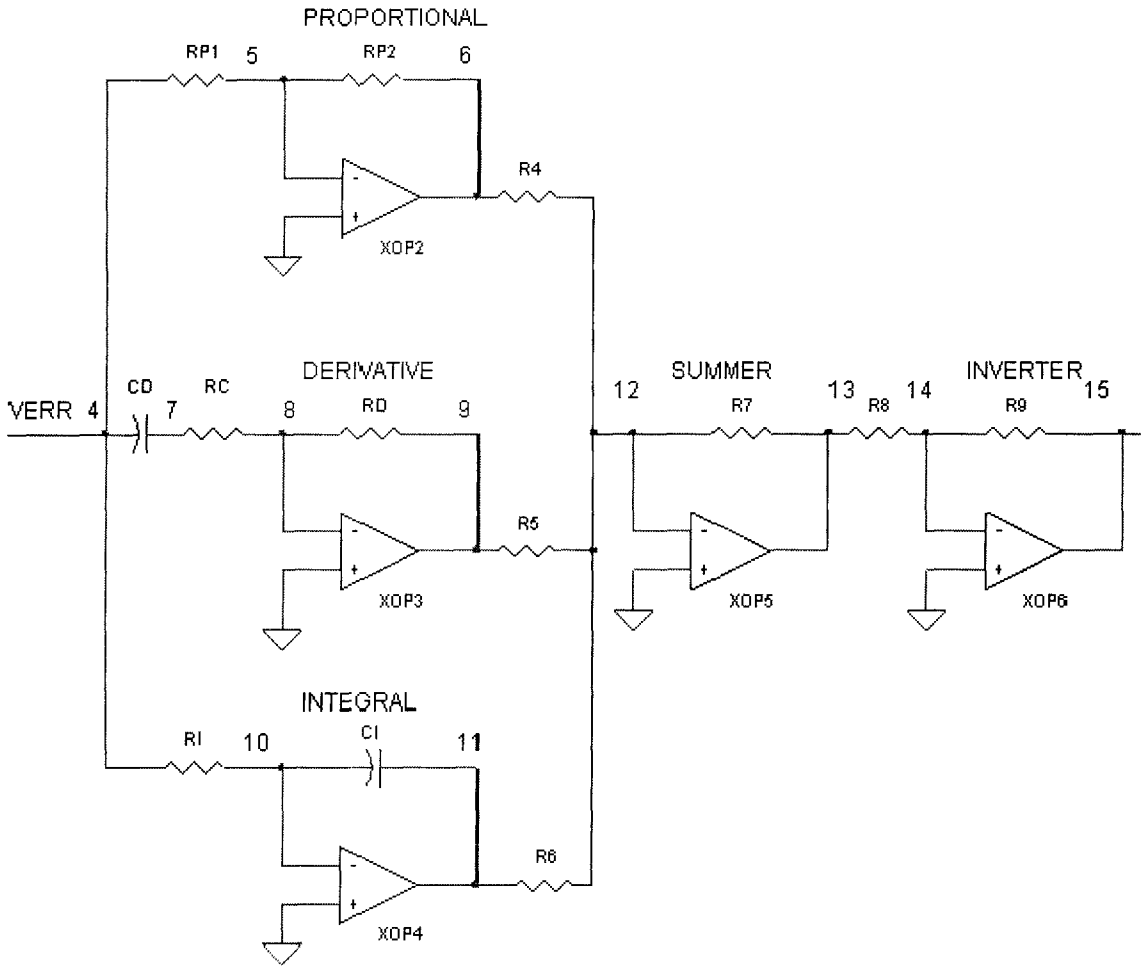

Figure 23: PID circuit [SPICE]

To create the controller gains desired, $K_i = \frac{-1}{R_I C_I}$, $K_p = \frac{R_4}{RP_2}$, and $K_d = -R_D C_D$.

Without the derivative control, the circuit is somewhat simpler. A less complex implementation, which uses only two op-amps, is given in Figure 24, along with the corresponding gain values.

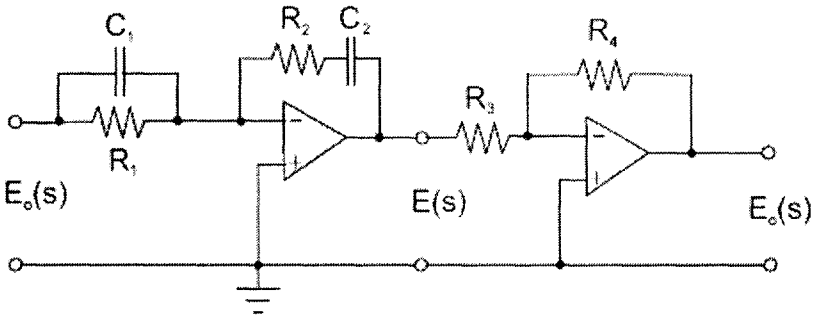

Figure 24: PID controller circuit [4]

$$\text{where } K_p = \frac{R_4(R_1C_1 + R_2C_2)}{R_3R_1C_2},$$

$$K_i = \frac{R_4}{R_3R_1C_2}, \text{ and } K_d = \frac{R_4R_2C_1}{R_3}.$$

Looking at Figure 15, the control circuit noise and thermo-mechanical noise both act as disturbances, and thus can controlled effectively by PI control. However, the Capacitive Sensor circuit noise is in the feedback path, and cannot be removed by the control circuit, so it is the most influential noise source. Show how switching speed is traded off as the capacitive sensor circuit noise increases.

4. Noise analysis

4.1. Noise in integrated circuits

When dealing with extreme accuracy in electrical circuits, electrical noise becomes the limiting factor. Electrical noise is caused by small fluctuations in voltage and current due to the discrete nature of electron flow. Noise gives a lower limit on the size of signal that can be amplified, and an upper limit on useful gain before saturation.

This device has four main sources of noise: 1) external vibrational noise, 2) Brownian noise, 3) thermal mechanical noise, and 4) noise in applied electrical signals. The first two can be reduced effectively by vacuum packaging, however the thermal mechanical and applied noise are more difficult to reduce to acceptable levels.

Shot noise

Shot noise is a property of the randomness of carrier movement across a junction. The external current is actually an average of many independent current pulses

$$\overline{i^2} = \overline{(I - I_D)^2}$$

If we model the current random independent pulses with an average value of I_D, then the mean-square value of the noise current is

$$\overline{i^2} = 2qI_D\Delta f(A^2) \quad [10]$$

Where q is the electronic charge (1.6×10^{-19} C) and Δf is the bandwidth in hertz. This equation is only valid as long as the frequency is comparable to the inverse of the carrier transit time. The effect of the noise can be modeled by a current generator shunting the device, with a Gaussian probability-density function .

The standard deviation of the Gaussian is the mean-square value, thus

$$\sigma^2 = \overline{i^2}$$

This will give an effective limit on the noise amplitude of +/-3σ. 99.7% of the time the noise will be within this limit .

Thermal Mechanical Noise

Unlike shot noise, thermal mechanical noise is independent of current flow. It is due to the random thermal motion of the electrons in the material and is directly proportional to the absolute temperature T:

$$\frac{1}{2}k\langle X^2\rangle = k_b T$$

Where k_b is Boltzmann's constant and $\langle X^2\rangle$ is the RMS value of the thermal mechanical noise.

In our device, the thermal mechanical noise is a dominant factor in the choice to use feedback control. Since the RMS noise goes up exponentially as the pull-in voltage is lowered (Figure 25), we can see that increasing the pull-in voltage will dramatically increase the device noise performance.

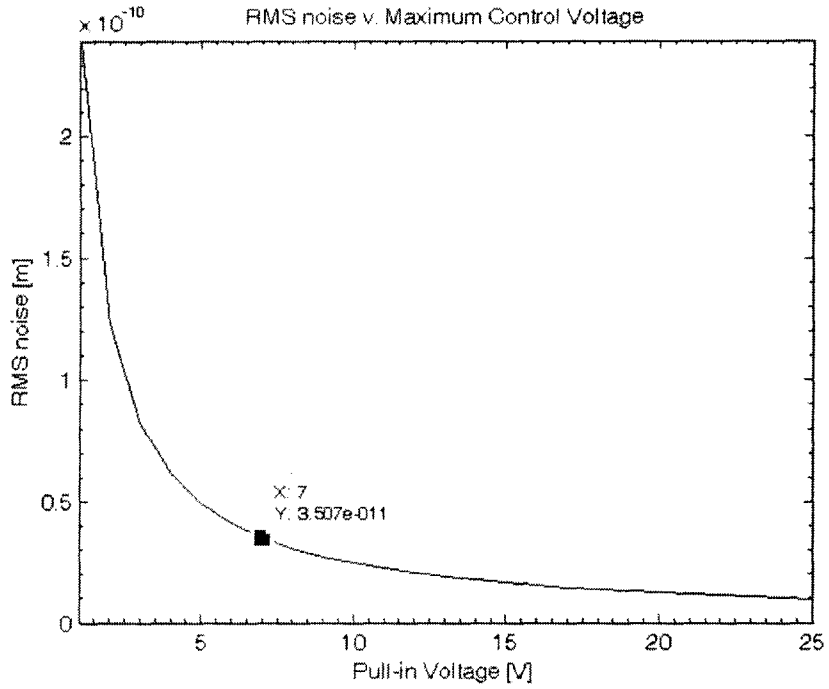

Figure 25: RMS noise for varying pull-in voltage

Given the 5V actuation voltage, we get an RMS noise value of 0.5Å for the three-electrode device, which is below the 0.7Å maximum noise specification for open loop control. However, this excludes the effects of electronic noise, which will cause the device to exceed the noise limits for meeting specifications. Thus, feedback control will be necessary.

4.2. Noise model

An outline of the Simulink control model is given in Figure 26 and the actual model is given in Appendices A and B.

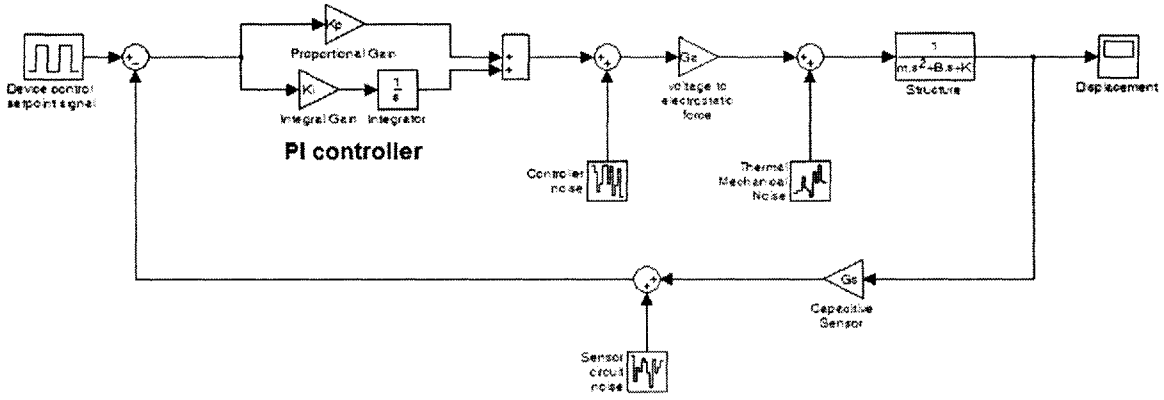

Figure 26: Simulink model of device noise

The thermal mechanical noise can be calculated based on the equation given in the previous section, and is dependent on the Temperature.

$$\frac{1}{2}k\langle X^2\rangle = k_b T$$

The thermal noise was modeled as band-limited white noise over the entire bandwidth of the system. The bandwidth of the system is the -3dB point, 2.9 x 10^5rad/s. The power spectral density of thermal noise is

$$Sn(f) = \frac{\hbar f}{2\left(e^{\frac{\hbar f}{kT}} - 1\right)}$$

where $\hbar$=6.6 x 10^{-34} J·s and k=1.38 x 10^{-23} J/K.

The capacitive sensor circuit noise will be calculated in the next section.

4.3. Noise in capacitive sensor circuit

The control circuit noise is only amplified by the control noise, and the thermal-mechanical noise only affects the structure. The sensor circuit noise, however, is in the feedback path, and is therefore the main electronic noise that must be dealt with (see Figure 26). A detailed model of the sensor circuit noise follows.

In any integrated circuit, the main noise sources are usually Johnson noise from resistors and op-amp noise. The noise model for the capacitive sensor circuit is in Figure 27.

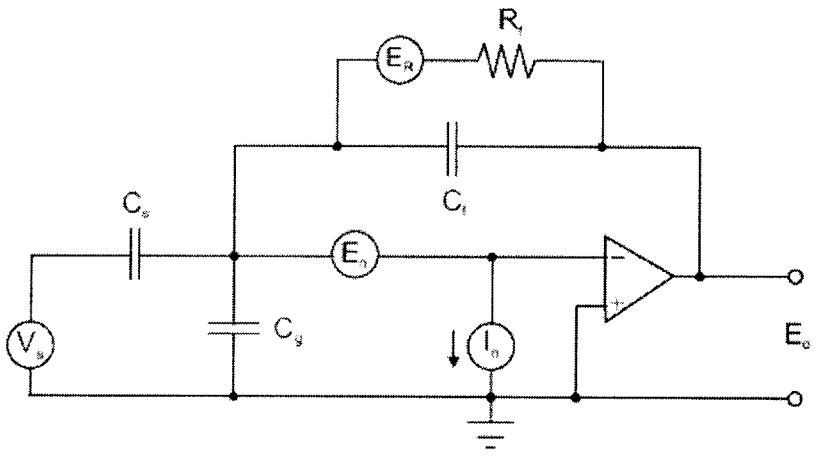

Figure 27: Capacitive sensor circuit with noise models

In this circuit, the maximum E_0 should be less than 5V for CMOS compatibility, where

$$E_0 = V_z \frac{C_s j\omega_s}{C_f j\omega_s - 1/R_f} \text{ [4].}$$

To reduce the op-amp noise in the external preliminary circuit, an ultra low noise op-amp can be used. After some research, I have chosen to use the CLC425 Ultra Low

Noise Wideband Op-amp to reduce the circuit noise in external testing. Its noise characteristics are given in Table 3.

	Input Voltage Noise $[\text{nV}\sqrt{Hz}]$	Current Noise $[\text{pA}/\sqrt{Hz}]$
Traditional op-amp	4.05	1.7
Ultra low noise op-amp	1.05	0.8

Table 3: Op-amp noise characteristics

The total noise is:

$$E^2_{n0} = \left| \frac{E^2_n \Delta f (1/R_f + j\omega_s C_s + j\omega_s C_g + j\omega_s C_f)}{1/R_f + j\omega_s C_f} \right|^2 + \left| \frac{\sqrt{4k_b T R_f \Delta f}}{1 - j\omega_s C_f R_f} \right|^2 + \left| \frac{I_n^2 \Delta f}{1/R_f + j\omega_s C_f} \right|^2$$

I simulated this circuit in SPICE and built it with the PI control circuitry, and found that the ultra-low noise op-amp visibly reduced the circuit noise, however full tests were impossible without the device in the loop.

A plot of the noise during a given simulation time for the system is given below in Figure 28. The modeled capacitive sensor will resolve a change in capacitance of 5.2 x 10^{-17}F, which corresponds to a displacement of 2.5pm.

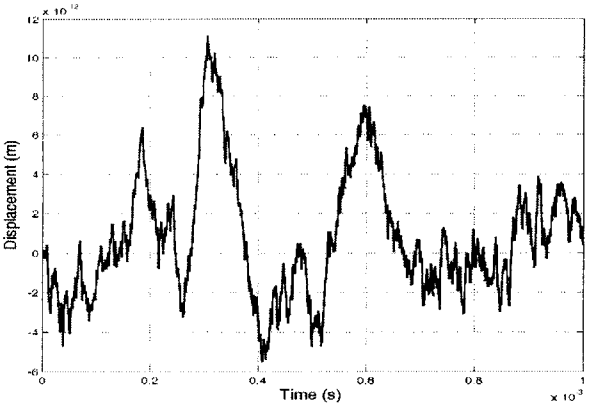

Figure 28: Noise in simulated system

5. Experimental apparatus for testing integrated optical devices

5.1. Equipment set-up

Integrated optical device testing requires efficient coupling of light into and out of 300-800nm wide waveguides, with relative ease in navigating between waveguides and flexible wavelength input of light for spectral testing. I have built an equipment apparatus that is useful in measuring optical properties such as coupling efficiency, spectral response, and mechanical speed of integrated optical devices. In addition, the apparatus can be used for measuring the optical switching characteristics of the MEMS bridge in the devices studied in this thesis. A schematic of the equipment is given in Figure 29. Slight modifications will be made depending on the measurements being taken.

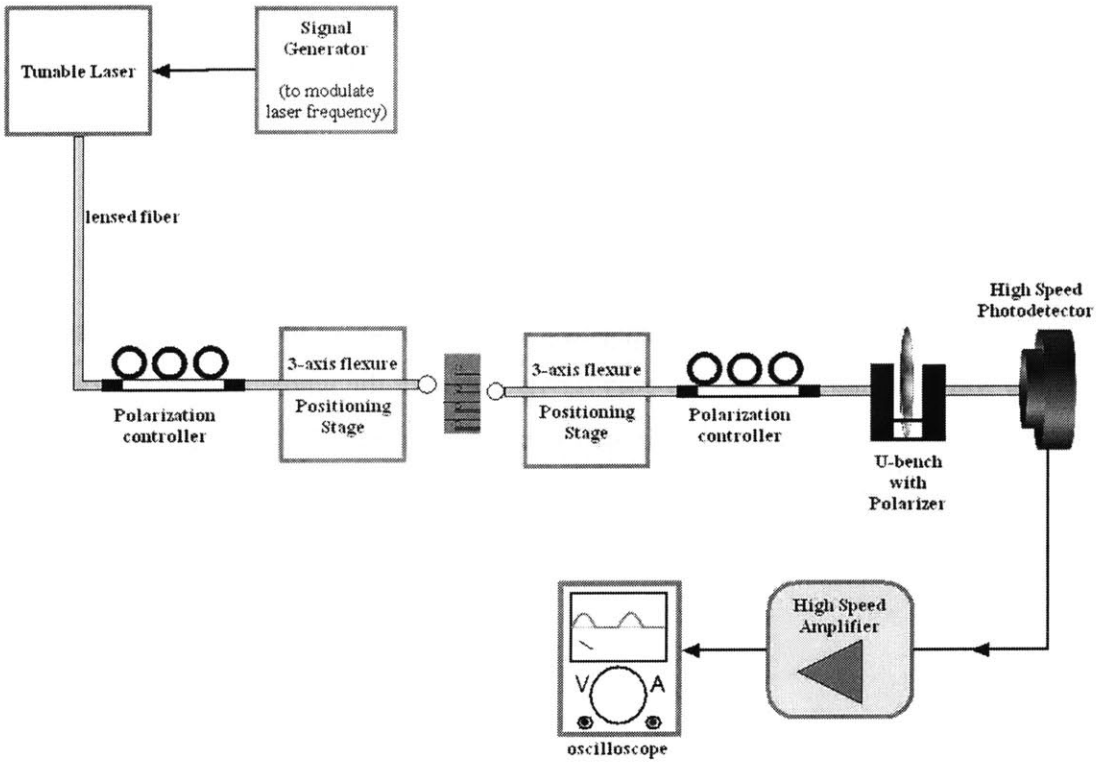

Figure 29: Test equipment set-up

Light from a tunable laser is sent through a three-paddle polarization controller and a lensed fiber, which is focused onto the selected integrated waveguide of the device under test. A 3-axis high-precision stage and a piezoelectric controller are used to focus the light to within several nanometers precision for optimal coupling efficiency. The light output by the device under test is then collected using another lensed fiber and polarization controller, and measured by a high-speed photodetector. The photodetector output must be amplified via a high-power amplifier in order to be viewed on an oscilloscope. This apparatus will mainly be used for ring resonator testing, but is adaptable to virtually any optoelectronic device.

Maximizing the coupling efficiency of the light into the integrated waveguides requires precision and depends on many factors. The lensed fiber tip must be aligned within a half micron of the center of the waveguide, the polarization into the waveguide must be optimized for that waveguide, and the polarization of the collected light from the device must be adjusted to match the requirements of the photodetector.

5.2. Alignment

The devices were mounted on an aluminum platform between the two nanopositioning stages, and a tube microscope was set-up above the wafer edges (see Figure 30) with translation stages for easy navigation over the whole wafer die. This makes it possible to image all of the devices in order to choose the best one or to explain device failures, and also allows approximate alignment of the lensed fiber to the integrated waveguide.

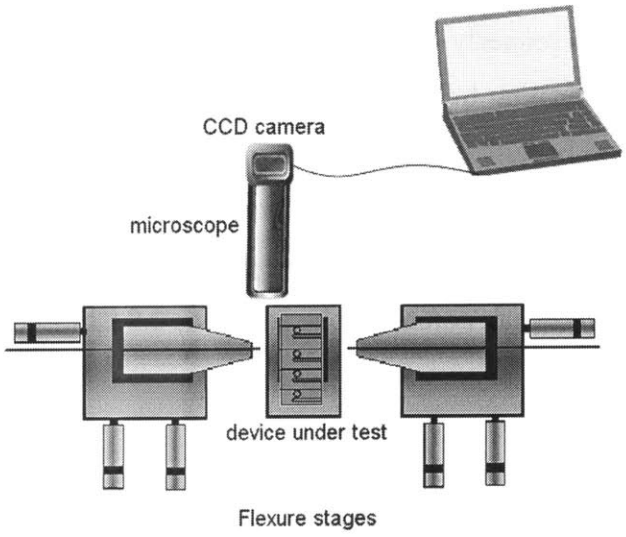

Figure 30: Device alignment equipment

The lensed fibers used had a beam waist at a distance of 3.5 microns from the fiber tip. With a normal objective lens, the coupling distance from the tip varies greatly depending on the wavelength of light used . The Nanonics lensed fibers, however, have the advantageous property of having very small changes in working distance with varying wavelength. Thus, they make it possible to measure the spectral performance of photonic devices across nearly the whole range of the tunable laser. It was for this reason that a lensed fiber was used for both light input and collection from the devices.

Another advantage of the relatively wavelength-independent property of the lensed fibers is that visible light laser diodes can be used to initially align the fiber tip to the waveguide on the device, without having to accommodate for the differences in beam focus due to diode having a much smaller wavelength than the IR range of the tunable laser, and thus eliminating the need for several expensive IR-sensitive CCD cameras. This technique for alignment involved attenuating the laser diode light until the focus cone was easily visible, then carefully adjusting the height of the lensed fiber near the device edge until it was half the height of the waveguide (150nm) above the silicon. The x axis was then aligned to be directly in front of the desired waveguide, and the y axis was adjusted visually to the working distance of the fiber tip.

Figure 31 shows a properly aligned fiber tip to waveguide. Notice that the focused cone of light emanating from the tip does not scatter onto the top of the wafer surface, does not expand beyond its waist, and does not saturate the CCD camera. The tip is 3.5 microns away from the waveguide, where the beam has a width slightly less than 1 micron, almost the exact width of the waveguide. Thus, the insertion loss from the fiber to waveguide end facet can potentially be as low as 0.8dB/facet, for an ideal device model.

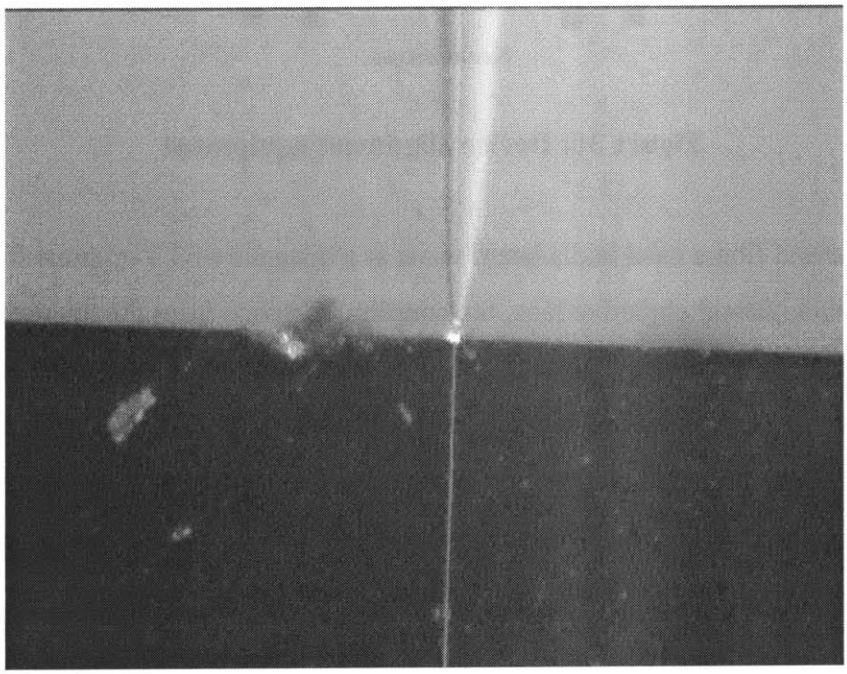

Figure 31: Aligned fiber tip and waveguide

To verify proper alignment, the edge of the waveguide was imaged, and then the position was perturbed slightly to find the best coupling. An IR sensitive camera was then used to image the edge facet, and moved the 3-paddle polarization controller to find the best polarization state for the waveguide.

The same rough alignment procedure was used for the through and drop waveguides on the other side of the wafer die; however, it was impossible to image the end facets of the input side without moving the first fiber tip. Instead, the two CCD

cameras were used to visually align the fiber along all three axes. The input light was then switched to the IR laser, and the polarization and position were adjusted while reading the output at the photodetector.

5.3. Wafer edge facets

When the wafer is cleaved, the waveguide ends tend to break off at different random places, as depicted in Figure 32. Some of the waveguides protrude from the edge, making coupling into the waveguide easier. Other waveguides break off further into the wafer, and experience shows that light will not couple into waveguides that are recessed by more than 3 microns.

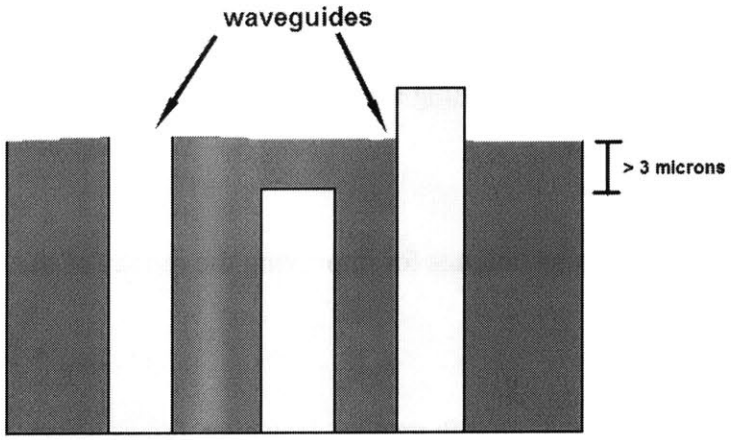

Figure 32: Cleaved waveguide edges

The CCD cameras were designed to magnify the device enough to evaluate the usability of each waveguide end facet, and it was found that, for the initial devices tested, only 25-30% of the waveguides were acceptable at both sides of the wafer die. Figure 33 is an SEM image of a good waveguide end facet.

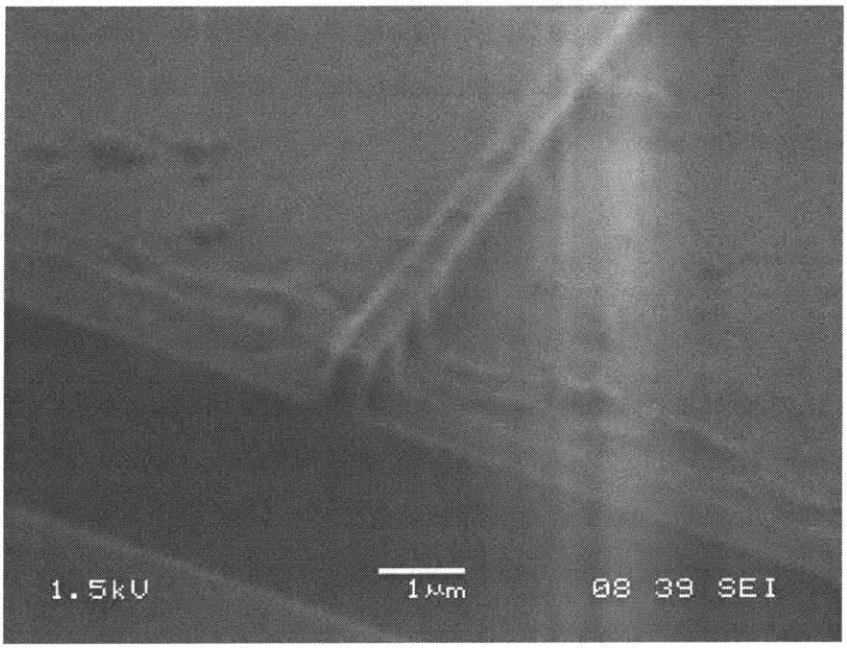

Figure 33: SEM image of one waveguide edge

Because the device wafer was cleaved, the end facets were also not all as flat as that shown in Figure 33. The positioning stages do not have angular adjustment, so this creates added insertion losses.

There are two known techniques for improving the quality of the waveguide edge facets:

- Polishing produces very smooth results. However, this is a very delicate process and can ruin the waveguides. Professor Kimerling's group at MIT has developed methods for improving the optical coupling capacity of integrated silicon waveguides through fine polishing techniques.
- Diesaw assisted cleaving is a fabrication post-process developed at MIT that involves partially cutting through the substrate with a diesaw, then cleaving at these perforations. The process flow is given in Appendix C. This technique produces much better cleaving results and is useful in our ring resonator tests; however, it will not work with the MEMS devices because the wax layer that is required would destroy the bridges.

5.4. Polarization Dependence

Consider a wave propagating in the z-direction with E_x and H_y components only. From Maxwell's equations, we can show that the propagation constants are different in the x- and y-directions for a nonsymmetrical waveguide. The fabricated waveguides used in our devices have a rectangular cross-section and are therefore polarization dependent. Figure 34, from [12], shows the polarization characteristics for a similar InGaAs waveguide. As can be seen from the graph, the TE mode has a lower effective index than the TM mode for waveguide widths below 1.5 microns. An interesting result of these curves is that, at 1.5 microns, the waveguide would be polarization independent.

For our devices, operating in single-mode, polarization independence is impossible, and we can deduce that the TE mode will give better results.

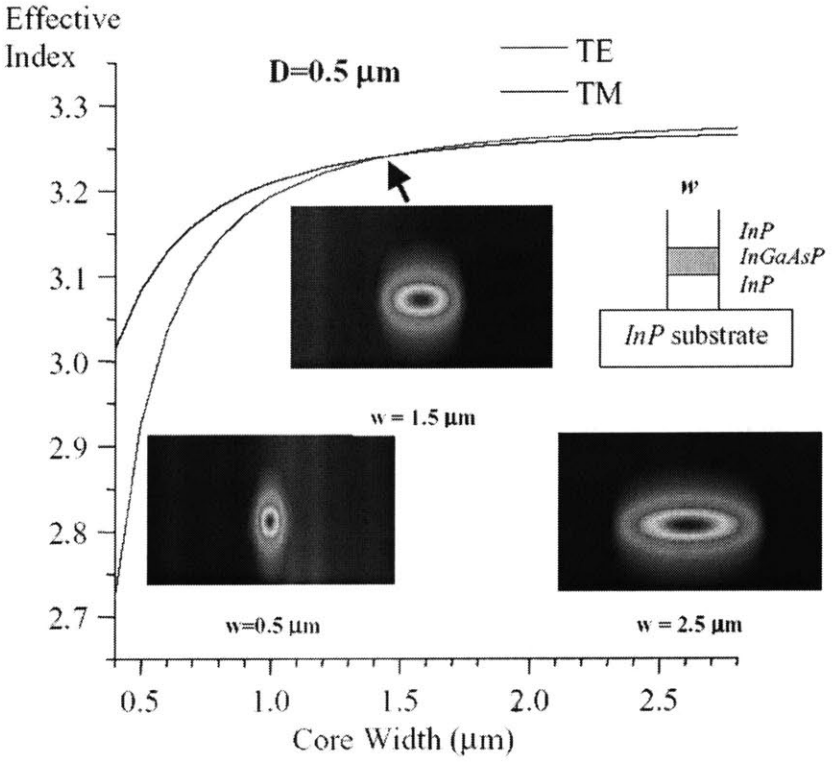

Figure 34: Waveguide polarization sensitivity [12]

In order to achieve coupling efficiency, the laser output polarization must be linearized and oriented correctly with the polarization controller such that the TE mode matches with the waveguide dimensions.

5.5. Ring resonators

The rings have a transfer function nearly identical to that of a Fabry-Perot cavity, with a free spectral range (FSR) dependent on the optical length

$$FSR = c / n_g L_r$$

where c is the speed of light, n_g is the group index, and L is the optical length. The bandwidth of the response is given by this parameter and the coupling coefficient, K.

$$Bandwidth = K(\frac{FSR}{\pi\sqrt{1-K}}) \text{ [9]}$$

The quality factor of the spectral peaks, Q, is simply the FSR divided by the bandwidth.

5.6. Optical performance tests

The first device tests were done for optical ring resonators without MEMS. The design parameters for the devices are given below in Figure 35. The laser was stepped through a range of wavelengths (1490nm-1570nm) and the optical output at the photodetector was measured for each step.

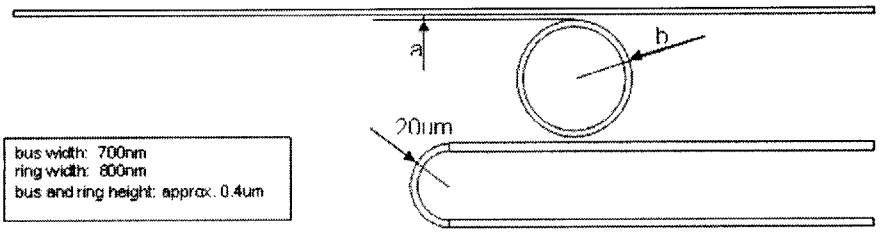

Figure 35: Ring resonator design

The high-speed photodetector has a voltage output of

$$V_{out} = Power \times \Re(\lambda) \times R_{Load}$$

where $\Re(\lambda)$ is the responsivity of the photodetector, which was measured to be 0.94A/W. At 1550nm and 12mW output power from the laser, with a 50Ω terminating resistance, the voltage at the photodetector should be 564mV. 598mV was measured for light directly from the laser to the photodetector.

Next, the light was sent through the polarization controllers and three fiber connectors. 97% of the light reached the photodetector; therefore the insertion loss for the fibers and connectors is 3%.

To deduce the coupling efficiency of the lensed fibers, two fibers were aligned tip-to-tip (Figure 36), and the output was measured. The rough alignment collected 58.8% of the light, and fine alignment along all three axes collected 70% of the laser light.

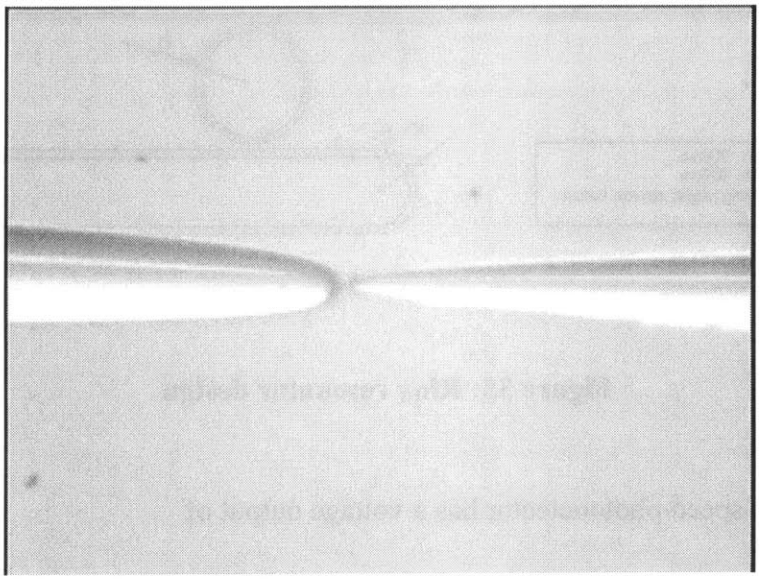

Figure 36: Fiber to fiber coupling

The next step was to measure the light attenuation at the device through port. After alignment, the output at the photodetector was almost negligible, and polarization adjustments did not improve the measurements. Both the through and the drop ports collected less than 2% of the incoming light at 1550nm, and many of the devices would not couple light at all. Varying the wavelength would not improve performance, as the lensed fibers were designed for light at 1550nm. The wafer tested suffered very low yield and high attenuation of light through the waveguides.

The spectral analysis measurements could be taken faster with the use of an Optical Dispersion Analyzer, which steps through a range of wavelengths and displays the spectral properties. However, by automating the measurements via GPIB control, the time for measurement becomes less important as it no longer requires constant attention.

5.7. Losses

The experimental optical losses in the waveguide through bus are due to coupling losses, material absorption inside the waveguide, and scattering due to waveguide

imperfections. The lower limit for coupling loss from the waveguide end facets, as discussed previously, is 0.7dB/facet, but was greater for end facets that were rough, tilted, or heavily recessed into the substrate.

As mentioned earlier, the waveguide propagation loss is mainly determined by free-carrier absorption and scattering at bulk and surface imperfections, given by γ. Transmission of optical power in the guide is given by:

$$P(z) = P(0)e^{-\gamma z},$$

which gives a loss in the waveguide loss in dB/cm, of $4.3\,\gamma$ [dB] [13].

Our devices are designed to have a propagation loss of approximately 0.4dB/cm, thus the total loss for an 8mm wide wafer die with 1550nm light and reasonable end facets could be as low as 2dB.

The observed losses in the waveguides were much higher than predicted. The additional loss was likely due to fabrication imperfections and poor quality of the end facets. We can see in Figure 33 that the quality of the waveguide is not great. These imperfections will contribute to additional scattering losses.

Figure 37 shows a microscope image of one device which has discontinuities in the waveguides (circled) and particle contamination (arrow). Both of these imperfections were found on many of the devices and contributed to the low yield.

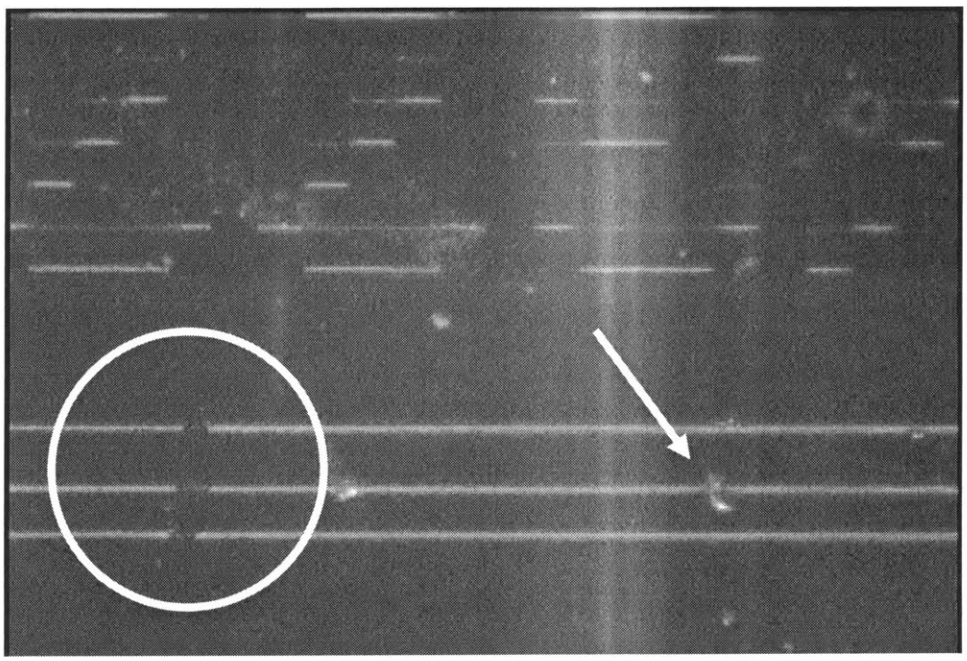

Figure 37: Waveguide imperfections

5.8. MEMS speed tests

The test setup can also be modified to measure the speed and optical characteristics of the switching using MEMS. This step has not been carried out yet, but is planned for the near future steps in this research. Probe tips will be connected to the MEMS bridge of the device, and an actuation signal can then be applied. The optical output will be measured by an ultra wideband oscilloscope, which accepts fiber input and must be triggered by either the optical signal or the device actuation signal. The MEMS bridge will be given a square wave voltage, and the resulting optical output will be measured to determine the switching speed. Figure 38 is the schematic of this testing set-up. Improved device design with a lower actuation voltage will allow for shorter rise and fall times of the switching device.

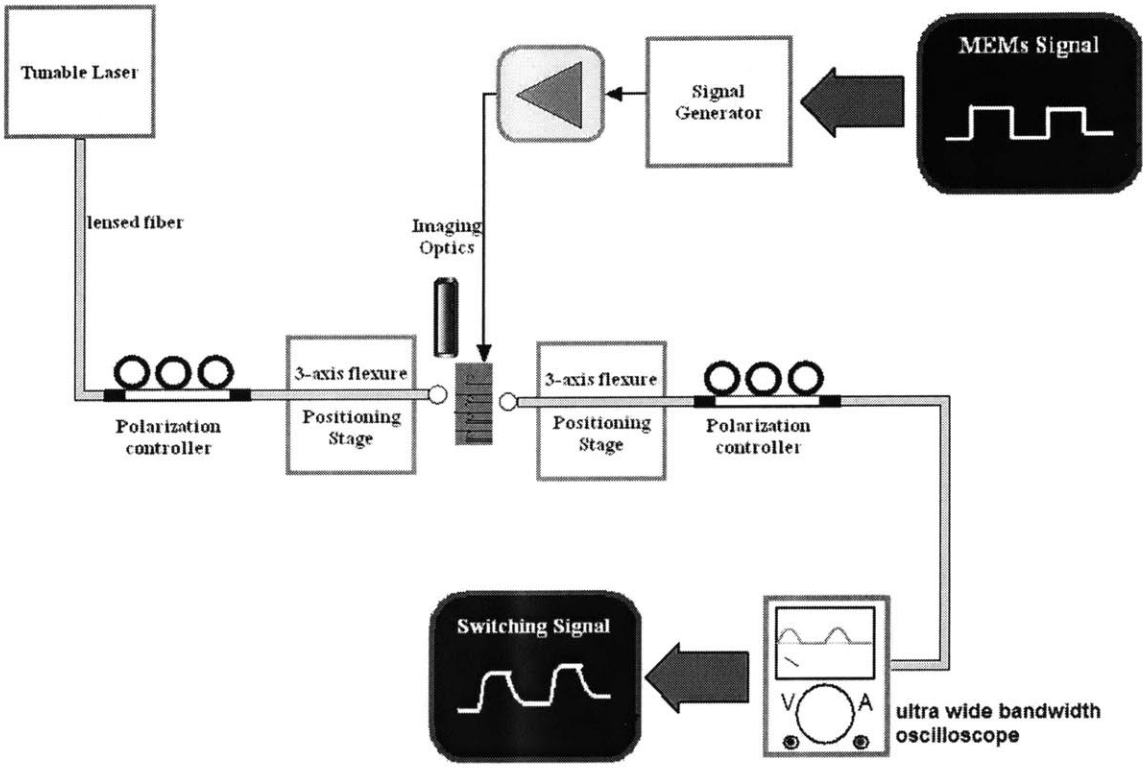

Figure 38: MEMS switching speed tests

In previous attempts at MEMS speed measurements [2], the measuring oscilloscope and the amplifiers limited the measurements to 8kHz. Thus, deterministic MEMS speed results were unattainable. Neilson used high-voltage amplifiers at the actuation signal and at the photodetector output.

With the configuration shown here, the actuation signal can be amplified by a fast op-amp, which has only a 5ns speed limit. The photodetector and the high-voltage amplifier are replaced by an ultra wide bandwidth oscilloscope. This oscilloscope accepts an optical input which will be triggered by the actuation signal. Thus, the speed measurements of the MEMS bridges will not be limited by the measurement equipment.

6. Conclusions and future work

6.1. Conclusion

The tunable wavelength-selective MEMS-controlled ring resonator filter is a useful integrated photonics device, not only for the EPIC project under which it is being developed, but also in telecommunications applications, or in variable optical attenuation devices. The filter has been designed with a tuning range of 30nm, covering approximately one communication band. It would be capable of tuning at speeds on the order of microseconds, which is sufficient for most applications. Because of the exponential nature of the dependence, even slightly less stringent specifications would result in much easier control circuitry. I showed that the control is feasible and designed circuitry for position control and fast actuation. I developed a testing apparatus for integrated optical devices and showed its use in several applications.

6.2. Future work

The first goal of future work on this project will be to test the newly fabricated MEMS devices. Then, a three-electrode sensor will be fabricated and tested for precision, speed, and accuracy. For further analysis of the MEMS bridge dynamics, I will work with Professor Dennis Freeman to use Computer MicroVision to study the bridge motion with his MEMS Motion Analyzer. The control system implementation will need to be tested with the actual devices in the loop. Eventually, the capacitive sensor electrodes and circuitry will be monolithically integrated.

References

[1] Aksyuk, V. e. a. (2000). Lucent Microstar micromirror array technology for large optical crossconnects. SPIE MOEMS and Miniaturized Systems.

[2] Nielson, G. (2004). Micro-Opto-Mechanical Switching and Tuning for Integrated Optical Systems. Department of Mechanical Engineering. Cambridge, MA, Massachusetts Institute of Technology. **PhD**.

[3] Wong, Chee Wei (2004). Strain-tunable silicon photonic band gap microcavities in optical waveguides, Applied Physics Letters Vol.84, No.8.

[4] Baxter, L. K. (1997). Capacitive Sensors: Design and Applications. New York, IEEE Press.

[5] Senturia, S. D. (2001). Microsystem design. Boston, Kluwer Academic Publishers.

[6] Tewari, A. (2002). Modern Control Design with Matlab and Simulink. New York, John Wiley & Sons, Inc.

[7] Van de Vegte, J. (1994). Feedback Control Systems, Third Edition. Englewood Cliffs, NJ, Prentice Hall.

[8] Jones, R. V., and J.C.S. Richards (1973). "The design and some applications of sensitive capacitance micrometers." Journal of Physics E: Scientific Instruments: 589-600.

[9] Haus, H. A. (2004). Waves and Fields in Optoelectronics. Marietta, OH, CBLS

[10] Gray, P., and Meyer, Robert G. (1993). Analysis and Design of Analog Integrated Circuits, Third Edition. New York, John Wiley & Sons, Inc.

[11] Dorf, R. C., and Bishop, Robert H. (2001). Modern Control Systems. New Jersey, Prentice Hall.

[12] Chin, M. K. (2003). "Polarization dependence in waveguide-coupled micro-resonators." Optical Society of America.

[13] Bhattacharya, P. (1994). Semiconductor Optoelectronic Devices. Englewood Cliffs, NJ, Prentice Hall.

[14] Barwicz, T. Diesaw assisted cleaving process flow. Cambridge, MA.

Biography:

Laura Waller is from Kingston, Canada, and completed her Bachelor's Degree in Electrical Engineering at the Massachusetts Institute of Technology in June, 2004. She has worked at the Research Laboratory of Electronics at MIT, in the Speech Research Group, as an undergraduate researcher. She also completed an internship at the Queen's University Lightwave Systems Lab in Kingston, Canada. She spent one year studying Electrical Engineering at Cambridge University in England. After graduating from the M.Eng program, she will remain at MIT in the EECS Department to complete a PhD in the 3D Optics Lab.

Appendix A: Control system SIMULINK model

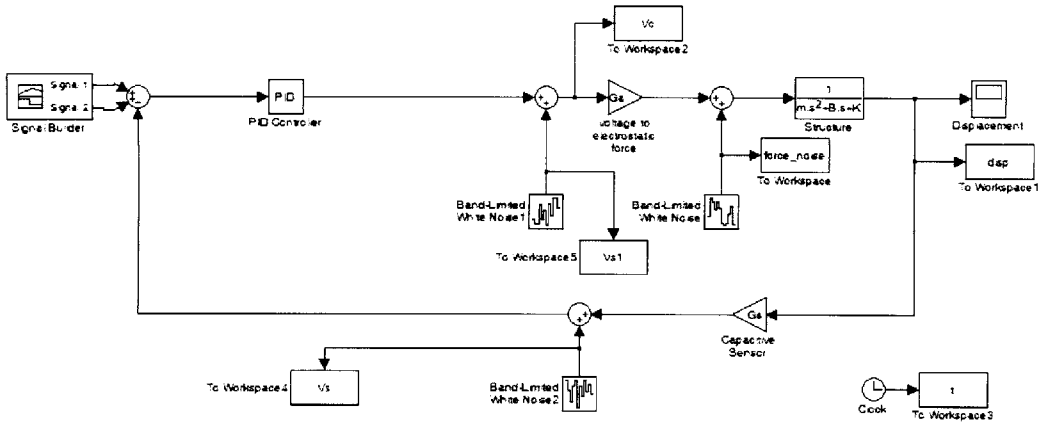

Simulation Parameters

Solver ode45	*ZeroCross* on	*StartTime* 0.0 *StopTime* .04
RelTol 1e-12	*AbsTol* auto	*Refine* 1
InitialStep auto	*FixedStep* auto	*MaxStep* 0.001

Clock Block Properties

Name	DisplayTime	Decimation
Clock	off	10

ToWorkspace Block Properties

Name	VariableName	MaxDataPoints	Decimation	SampleTime	SaveFormat
To Workspace	force_noise	inf	1	-1	Array
To Workspace1	disp	inf	1	-1	Array
To Workspace2	Vc	inf	1	-1	Array
To Workspace3	t	inf	1	-1	Array
To Workspace4	Vs	inf	1	-1	Array

Name	VariableName	MaxDataPoints	Decimation	SampleTime	SaveFormat
To Workspace5	Vs1	inf	1	-1	Array

TransferFcn Block Properties

Name	Numerator	Denominator	AbsoluteTolerance
Structure	[1]	[m B K]	auto

Continuous White Noise. Block Properties

Name	Cov	Ts	seed	VectorParams1D
Band-Limited White Noise	[(4*Kb*T*B)/2]	1/(band_mult*band)	[2153]	on
Band-Limited White Noise1	[Enos^2/130000]	1/(band_mult*band)	[8341]	on
Band-Limited White Noise2	[Enos^2/13000000]	1/(band_mult*band)	[297]	on

PID Controller Block Properties

Name	P	I	D
PID Controller	Kp	Ki	Kd

Appendix B: Thermal plant SIMULINK Model

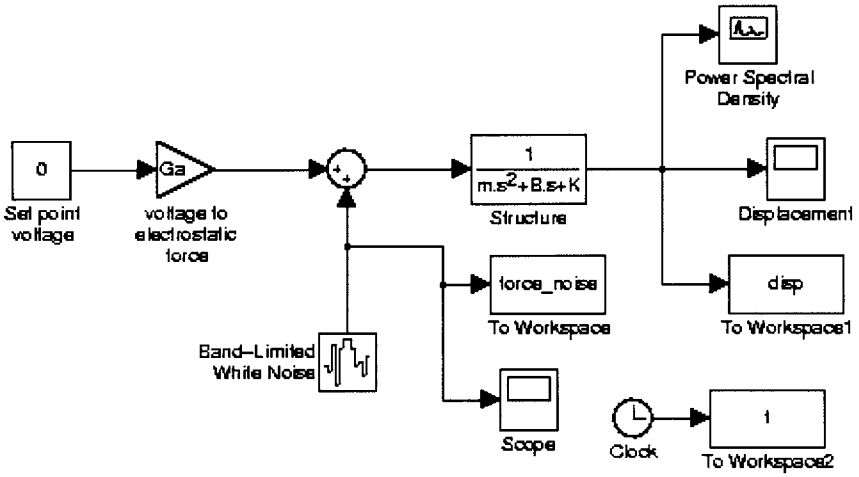

Simulation Parameters

Solver ode45	*ZeroCross* on	*StartTime* 0.0 *StopTime* .05
RelTol 1e-12	*AbsTol* auto	*Refine* 1
InitialStep auto	*FixedStep* auto	*MaxStep* .001

Clock Block Properties

Name	DisplayTime	Decimation
Clock	off	10

ToWorkspace Block Properties

Name	VariableName	MaxDataPoints	Decimation	SampleTime	SaveFormat
To Workspace	force_noise	inf	1	-1	Array
To Workspace1	disp	inf	1	-1	Array
To Workspace2	t	inf	1	-1	Array

TransferFcn Block Properties

Name	Numerator	Denominator	AbsoluteTolerance
Structure	[1]	[m B K]	auto

Continuous White Noise. Block Properties

Name	Cov	Ts	seed	VectorParams1D
Band-Limited White Noise	[(4*Kb*T*B)/2]	1/(band_mult*band)	[2563]	on

Power Spectral Density Block Properties

Name	npts	fftpts	HowOften	sampleT
Power Spectral Density	128	512	64	0.000001

Appendix C: Process flow for diesaw assisted cleaving of wavers